Available online at www.sciencedirect.com

SciVerse ScienceDirect

Geochimica et Cosmochimica Acta 75 (2011) 6439–6460

Geochimica et Cosmochimica Acta

www.elsevier.com/locate/gca

Investigation into the petrogenesis of Apollo 14 high-Al basaltic melts through crystal stratigraphy of plagioclase

Hejiu Hui *, Jocelyn G. Oshrin, Clive R. Neal

Department of Civil Engineering and Geological Sciences, University of Notre Dame, Notre Dame, IN 46556, USA

Received 11 February 2011; accepted in revised form 9 August 2011; available online 16 August 2011

Abstract

The petrogenesis of Apollo 14 high-Al basaltic melts was studied using crystal stratigraphy, which involves textural (crystal size distributions — CSDs) and chemical analyses (electron microprobe and laser ablation inductively coupled plasma mass spectrometry). The samples studied here include pristine basalt 14072 and basaltic clasts from breccia 14321, and impact-generated crystalline samples 14073, 14276 and 14310. Plagioclase was the focus of this study because of its relatively high modal abundances and because it was on the liquidus for much of the melt cooling histories. Plagioclase crystals were analyzed (core-to-rim compositions where possible) to test and refine petrogenetic models based upon whole-rock compositions (Groups A, B, and C designations) and to investigate basalt 14072 and impact-melt crystallization. Textural studies have shown that each basalt group has distinctive plagioclase CSDs, which are in turn distinctive from those of the impact melts. Evolution of the individual basaltic melts was studied by comparing the equilibrium-melt compositions (calculated from plagioclase compositions using relevant partition coefficients) to fractional crystallization (FC) and assimilation and fractional crystallization (AFC) models. Petrogenetic modeling of trace elements in Group A basalts revealed that petrogenesis continued beyond 40% total crystallization required to model whole-rock compositions, and that there were open-system processes that affected the magma during plagioclase crystallization. Petrogenetic modeling of pristine high-Al basalts (14072 and Groups A, B and C) using trace elements shows that the equilibrium-melt compositions do not fall on a single AFC or FC trajectory. This is consistent with fluctuating degrees of assimilation (i.e., variable *r*-values) and/or variable assimilant compositions during petrogenesis. Petrogenetic modeling reveals that the impact melts experienced only closed-system fractional crystallization. This work demonstrates the importance of crystal stratigraphy in revealing the intricacies of lunar basalt petrogenesis.

1. INTRODUCTION

The Apollo 14 high-Al basaltic samples ($Al_2O_3 \geqslant 11$ wt.%, compared to 7–11 wt.% of other mare basalts; e.g., Neal and Taylor, 1992) were collected from the Moon's Fra Mauro region in February 1971, which is composed mostly for impact ejecta from the Imbrium basin. Two different origins of these high-Al basaltic melts were identified: volcanic eruption, referred to as "pristine", meaning the sample is free of meteoritic components and formed solely via endogenous lunar processes; and meteorite impact, the generated melts referred to as "impact melt", which potentially contains meteoritic signatures. Though most of the samples collected by the Apollo 14 mission are impact melts and breccias, several pristine basalts (e.g., 14053 and 14072) were returned and some of the breccias (e.g., 14321) contain pristine basaltic clasts. These pristine basalts have been determined to have three different ages (~4.3, ~4.1, and ~3.95 Ga; Papanastassiou and Wasserburg, 1971; Mark et al., 1973, 1974, 1975; Dasch et al., 1987). Therefore, the Apollo 14 high-Al mare basalts provide geologic records of the Moon between the formation of lunar crust (~4.4 Ga) and the main basin-filling mare volcanism (<3.85 Ga; Shearer et al., 2006). Several models — including impact-generation (e.g., Snyder et al., 2000), varying degrees of partial melting of a single source (e.g., Dickinson et al.,

* Corresponding author. Tel.: +1 574 631 0478.
E-mail address: hhui@nd.edu (H. Hui).

0016-7037/$ - see front matter © 2011 Elsevier Ltd. All rights reserved.
doi:10.1016/j.gca.2011.08.015

1985; Shervais et al., 1985; Dasch et al., 1987), partial melting of a hybridized mantle (e.g., Hagerty et al., 2005), and fractional crystallization with assimilation (e.g., Neal et al., 1988, 1989a; Neal and Taylor, 1990; Neal and Kramer, 2006) — attempted to describe the origin and evolution of the Apollo 14 high-Al basalts. It was demonstrated that variable degrees of partial melting of a single source cannot yield the range of trace-element abundances measured in these samples (e.g., Dickinson et al., 1985; Shervais et al., 1985; Hagerty et al., 2005).

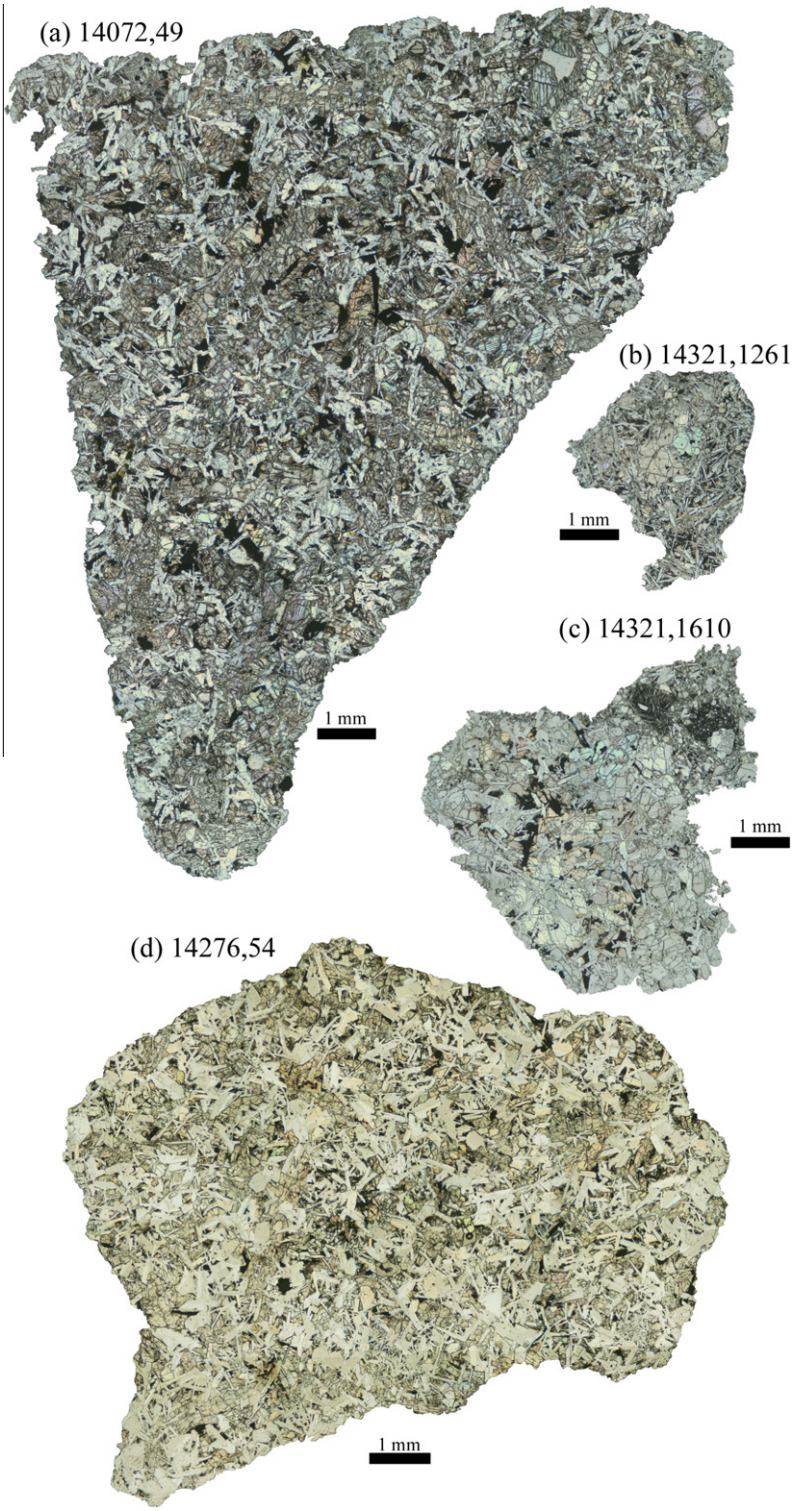

Fig. 1. Plane polarized light photomicrographs of (a) pristine basalt 14072.49, two basalt clasts (b) Group B basalt 14321.1261 and (c) Group C basalt 14321.1610, and (d) impact melt 14276.54.

On the basis of basalt ages and whole-rock incompatible-trace-element ratios (e.g., Nb/Ce) that are unaffected by fractional crystallization of observed phases, Neal and Kramer (2006) concluded that (1) the Apollo 14 high-Al mare basalts formed three different groups (A, B and C), thus indicating the basalts were derived from three distinct source regions (at three separate times); (2) basalt 14072 does not fall into any of these three groups, indicating the presence of a possible fourth (and poorly sampled) group at the Apollo 14 site; and (3) the pristine basalts are compositionally distinct from the Apollo 14 aluminous impact melts. Using the crystallization assemblage of each Apollo 14 basalt group estimated with the program *MELTS* (Ghiorso and Sack, 1995), Neal and Kramer (2006) hypothesized that Group A basalts could be generated by 30–40% closed-system crystal fractionation, but realized that the ranges of abundances and ratios of incompatible trace elements in Group B and C basalts could not have been produced by closed-system processes or assimilation of just a KREEP (K, rare earth elements (REE) and P rich; e.g., Meyer, 1977; Warren and Wasson, 1979) component as proposed by Neal et al. (1988, 1989a). Thus, assimilation of a component comprising a mixture of KREEP-rich quartz monzogabbros (QMD in Jolliff, 1991; hereafter referred to QMG) and granite (Warren et al., 1983a) was proposed to produce the array of measured whole-rock compositions with 25% fractional crystallization and 2.5% assimilation for Group B basalts, and 40% fractional crystallization and 4.8% assimilation for Group C basalts (Neal and Kramer, 2006). This "mixed" assimilant is reasonable given the association of KREEP and granite as documented in lunar samples, such as 15405 (Ryder, 1976).

Geochemical information (e.g., siderophile-element content, incompatible-trace-element ratio) can be used to differentiate pristine samples and impact melts (cf. Warren, 1993), as well as between different mare basalt groups (e.g., Neal and Kramer, 2006). The different groups of basalts experienced different petrogenetic process as revealed by the whole-rock incompatible-trace-element data (Neal and Kramer, 2006). However, the different petrogenetic histories are not reflected in distinct textural differences such that initially, some impact melts were classified as pristine basalts (e.g., Gancarz et al., 1971, 1972; Ridley et al., 1972; Longhi et al., 1972; Ridley, 1975; Neal et al., 1989b) (Fig. 1).

Crystal size distributions (CSDs), which measure the number of crystals of a characteristic size per unit volume of rock, can provide a quantitative measure of rock texture controlled by petrogenetic processes (e.g., Marsh, 1988). This quantitative method of textural analysis has been used to decipher the melt crystallization dynamics (e.g., Hersum and Marsh, 2007; Higgins, 2011a).

In this paper, crystal stratigraphy of plagioclase, which involves both textural (CSDs) and spatially resolved chemical analyses (major- and trace-element concentrations), were used to study the petrogenesis of Apollo 14 high-Al mare basalts (basalt 14072 and Groups A, B and C) and impact melts (14073, 14276, and 14310). Plagioclase is abundant in Apollo 14 high-Al basaltic melts (Table 1) and it was on the liquidus for much of their cooling histories (e.g., Papike et al., 1976). Hence, plagioclase crystals record much of the crystallization history and can be used to test and refine the petrogenetic models presented by Neal and Kramer (2006) on the basis of whole-rock data for each basalt group.

2. METHODS

Twenty-one Apollo 14 high-Al basaltic samples were used in this study for textural analysis, including eighteen pristine basalts (14072 and clasts from breccia 14321) and three impact melts (14073, 14276, and 14310). Ten of them were also analyzed for chemical compositions using electron microprobe and laser ablation inductively coupled plasma mass spectrometry, including eight pristine basalts (14072 and seven clasts from breccia 14321) and two impact melts (14073 and 14276).

2.1. Crystal size distributions (CSDs)

Crystal size distributions (CSDs) of plagioclase are used to distinguish unique crystal populations. CSDs measure the number of crystals of a particular size (i.e., a particular crystal length) per unit volume of rock and are generally plotted as the natural logarithm of the population density

Table 1
Modal mineralogies (vol.%) of the Apollo 14 samples in this study.

	14321 Clasts[a]	14072[a]	14073[a]	14276[a]	14310[a]
Olivine	0–16	2.5			Tr.[b]
Pyroxene	16–52	49.9	45	29	32.9–40
Plagioclase	18–45	38.3	50	64.6	50–59
Opaques		7.7			2.9–3
Ilmenite	5–16		2	1.2	1.8–3
Chromite	0–8				
Fe–Ni metal/Troilite	1–11		Tr.[b]	0.3	0.1
Glass and Silica		1.7		3.5[c]	4.4[c]–5.9
Silica	0–6				
Glass	0–22		Tr.[b]		
Phosphate			Tr.[b]	0.6	0.3

[a] Data sources: 14321 clasts: Neal et al. (1989b), 14072: Longhi et al. (1972), 14073: Gancarz et al. (1971), 14276: Gancarz et al. (1972), 14310: Gancarz et al. (1971, 1972), Longhi et al. (1972).
[b] Tr. = trace amounts present.
[c] Reported as "mesostasis".

versus the crystal size (e.g., Marsh, 1988). The intercept of the CSD curve represents nucleation density (i.e., $\ln(n^0)$), and the slope is a function of average crystal growth rate (G) and average crystal residence time in the system (τ) following the formula:

$$\text{CSD slope} = 1/G\tau. \quad (1)$$

In this study, CSDs of plagioclase were used to explore any textural differences among the pristine basalt groups, and between the pristine basalts and the impact melts.

Digital photomicrographs were made of the thin sections of all twenty-one samples using a Nikon petrographic microscope with a 5X objective under both plane and crossed polarized light. Using *Adobe Photoshop©*, the outline of each plagioclase crystal intersection (i.e., observed crystal surface through microscope) was traced and filled with a shade of gray. The entire image was then converted into an uncompressed 8-bit BMP format and processed by the program *ImageTool* (Higgins, 2000), which measured the length, width, roundness, and area of each crystal intersection on the thin section. The intersection length and width were used to convert the 2-D crystal intersection shape (i.e., the observed crystal shape on the section) into the most probable 3-D crystal habit (aspect ratios of long, intermediate and short dimension) with the program *CSDSlice* (Morgan and Jerram, 2006). The program *CSDcorrections1.37*, which considers the 3-D crystal habit, total measured area, average crystal roundness and intersection length (or width), was used to resolve the cut-section effect (i.e., the unlikely occurrence that the crystal is intersected at the exact center of its longest axis) and to estimate the true 3-D crystal size distribution (Higgins, 2000). Four to six bins per decade (i.e., logarithmic-size intervals for sizes that vary by a factor of 10) were used in the plot of CSDs depending on the total number of crystals ($\geqslant$200; Higgins, 2000).

The length of plagioclase crystals, which intersections can be precisely traced in *Photoshop©* is <0.1 mm. Therefore, the error arising from the outline of crystal intersection for intermediate-size crystals (i.e., 0.1–1 mm; see Section 3.1) is negligible. However, inaccuracy in the determination of population densities can potentially rise from the following three aspects (Higgins, 2000): (1) the counting statistics error (i.e., how many crystals counted in each crystal size interval), which can be minimized by making each interval contain at least 20 crystal intersections (Higgins, 2000; also see Section 3.1); (2) the probability that a crystal with a true size in one interval will have an intersection that falls in another different interval (this error is important for small size intervals; Higgins, 2000); and (3) the error associated with the conversion of crystal intersection length (or width) to true crystal size. In this study, the overall error of population density is less than 5% in the most intermediate-size intervals (i.e., 0.1–1 mm) using *CSDcorrections1.37* (Higgins, 2000).

2.2. Electron probe microanalysis

The thin sections of 10 high-Al basaltic melts were carbon coated, then analyzed on a JEOL JXA-8200 electron microprobe equipped with five wavelength-dispersive spectrometers, and a JEOL (e2v/Gresham) silicon-drift energy-dispersive spectrometer. Analyses were acquired using either the Probe for Windows or JEOL analysis software, and X-ray correction was performed using the CITZAF correction software (see Armstrong, 1995). Typical operating conditions for plagioclase analyses were 15 kV accelerating voltage and 25 nA current, using a defocused beam where practical (typically 5–10 μm diameter) with typical count times of 30 s on peak and 20–30 s on background. Standards used in the facility range from pure elements and oxides to simple or complex silicates and glasses recognized throughout the analytical community. The primary standards of a 10 element analytical setup for plagioclase were: Na, Si: Amelia albite; Mg: Shankland forsterite (synthetic); Al: Alaska anorthite; K: microcline; Ca: Gates wollastonite; Ti: synthetic TiO_2; Cr: synthetic Cr_2O_3; Mn: synthetic Mn_2SiO_4; Fe: synthetic fayalite (see http://xraysrv.wustl.edu/web/probe/probe2.html for more details). Primary standards were typically measured at the beginning of each day. During the run, primary standards were checked against each other, and Kakanui hornblende and other standards were used as secondary standards to check the calibration. The measurements were quantified using the Armstrong Phi-Rho-Z algorithm coupled with Henke and Heinrich mass absorption coefficients.

Backscattered electron (BSE) images were used to select analysis spots on the individual plagioclase crystals, as the images exhibit differences in total atomic weight, and thus highlight compositional zoning (Fig. 2a). In some areas X-ray maps were also used to identify locations for analysis (Fig. 2b). Two to six locations, which were free of fractures and inclusions, were chosen on each analyzed crystal. If zoning was apparent, measurements were taken from each zone; if not, measurements were taken from the rim and core on small crystals (<~0.2 mm in length), or the rim, core and some intermediate spots on larger crystals (>~0.2 mm in length). The detection limits were typically better than 500 ppm and the standard errors based on counting statistics during analyses were typically better than 1% for oxides >10 wt.%, 1–3% for oxides 1–10 wt.%, and 1–5% for oxides <1 wt.%.

2.3. LA-ICP-MS analysis

A 213 nm Nd-YAG New Wave laser ablation system in conjunction with a Thermo-Finnigan Element 2 high resolution magnetic sector inductively coupled plasma mass spectrometry (LA-ICP-MS) were used to analyze the trace elements in the plagioclase crystals at University of Notre Dame. Each crystal was analyzed in locations correlating with previous electron microprobe analyses so that the calcium concentrations (CaO weight percent measured by the electron microprobe, and ^{44}Ca abundances measured by LA-ICP-MS) could be used as an internal standard in each zone. Samples were ablated using the rastering method within distinct compositional zones of plagioclase crystals. The laser had a repetition rate of 5 Hz, a spot diameter of 30–40 μm depending on crystal size and zone, and 70–100% power output depending on crystal durability (i.e., how quickly the laser penetrated through the plagioclase

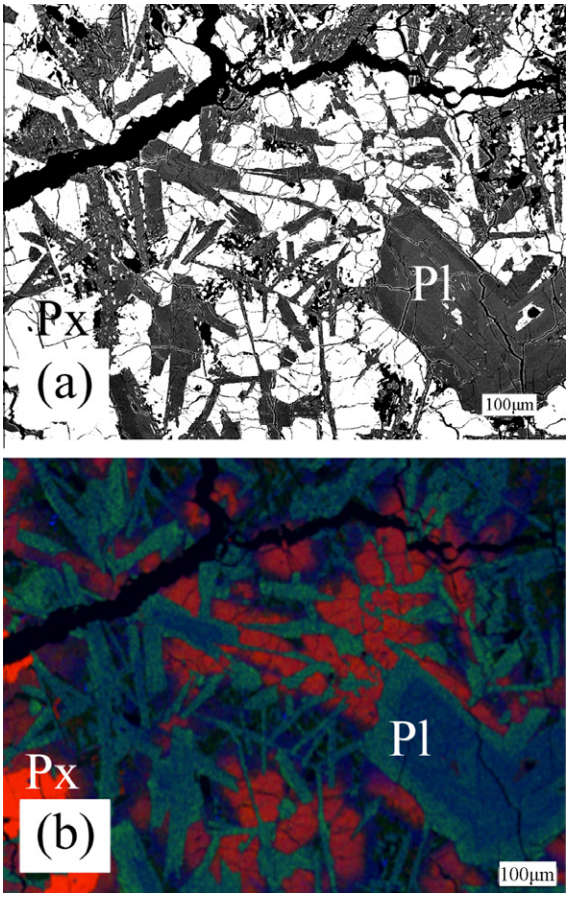

Fig. 2. Plagioclase zoning in sample 14321.1476 (Group C) illustrated by (a) a Backscattered electron (BSE) image and (b) an RGB image using the Mg, Na and Ca X-ray maps of the same location. Red indicates high Mg concentrations, green indicates high Na concentrations, and blue indicates high Ca concentrations. Px: pyroxene, Pl: plagioclase. (For interpretation of the references to colour in this figure legend, the reader is referred to the web version of this article.)

crystal on the thin section). Typical penetration depth is less than 20 μm per 60 s analysis. The ablated particles were transported into the ICP-MS by a helium–argon gas mixture with 0.7 l/min of He. The stability of the Element 2 ICP-MS allowed trace elements Ga, Sr, Y, Ba, La, Ce, Na, Sm, Eu, Gd, Dy, Er, and Yb to be measured in peak jumping mode with only one point quantified per mass. NIST 612 glass was used as an external standard to correct for instrument drift and ensure reproducibility in the measurements. The LA-ICP-MS data were reduced using the program *GLITTER*© (a software for the laser ablation microprobe, which provides the first real-time interactive data reduction for LA-ICP-MS analysis). The detection limits were better than 0.05 ppm for all trace elements except for Sr (better than 2 ppm). The standard errors based on counting statistics, natural concentration variations during ablation, and propagated errors including uncertainties in standard values during each analytical session were better than 5%. Furthermore, *GLITTER*© can be used to monitor whether incompatible-trace-element rich inclusions were ablated. When such inclusion is ablated, we can recognize a sudden change of incompatible trace elements and Ca concentrations in the time-resolved data. No such observations were made during our analyses.

3. RESULTS

All Apollo 14 samples studied here have a basaltic chemical composition (e.g., Gancarz et al., 1972; Longhi et al., 1972; Neal et al., 1989a). Textures range from ophitic to subophitic within each of three groups (A, B and C) of basaltic clasts from breccia 14321. All these basaltic clasts contain plagioclase (18–45 vol.%) and pyroxene (16–52 vol.%), with some having olivine phenocrysts (⩽16 vol.%) (Neal et al., 1989b). The major opaque oxide is ilmenite (5–16 vol.%), which generally occurs as subhedral laths and as irregular grains in mesostasis (Neal et al., 1989b). Accessory phases include chromite, troilite, Fe–Ni metal, SiO_2 and glass (Neal et al., 1989b). Rock 14072 is a porphyritic basalt with subrounded olivine phenocrysts (2.5 vol.%; Longhi et al., 1972). It is composed of pyroxene (49.9 vol.%) and plagioclase (38.3 vol.%) with accessory ilmenite, spinel, cristobalite, troilite and native iron (Longhi et al., 1972). Impact melt 14073, 14276 and 14310 are subophitic in texture. They consist predominantly of plagioclase (50–65 vol.%) and pyroxene (29–45 vol.%), with minor ilmenite, spinel, troilite, and Fe-metal (Gancarz et al., 1971, 1972; Ridley et al., 1972; Longhi et al., 1972). There is no "distinct" difference in textures between different basalt groups and between the impact melts and the pristine basalts, as shown in Fig. 1. The modal mineralogies are summarized in Table 1.

3.1. Textural analysis

A comparison of crystal size distributions of the pristine basalts and the impact melts shows that each compositional group occupies a distinct range of slopes with little overlap, while that of basalt 14072 falls in the range of Group C (Fig. 3, Table 2). The impact melts have plagioclase CSDs that also plot distinctly from the pristine basalts (Fig. 3, Table 2). The CSDs are truncated at 0.1 mm crystal length because that is the smallest crystal size that can accurately be identified and traced using the methods described above (see Section 2.1). Each crystal length interval increases by 56–68% depending on total number of crystals counted, so that each interval contains a sufficient number of crystals and there are no size bins without crystals—even in the larger sizes where there are fewer crystals. Having logarithmic crystal length intervals also minimizes the total number of size bins, which, in turn, reduces the errors associated with the slope and intercept measurements (Fig. 3).

3.2. Compositional analysis

Plagioclase major-element compositions in Apollo 14 high-Al basaltic melts are heterogeneous with a general Fe enrichment and anorthite depletion towards grain rims (Fig. 4a and b). Plagioclase grains analyzed in this study have a wide range of anorthite contents, especially rims

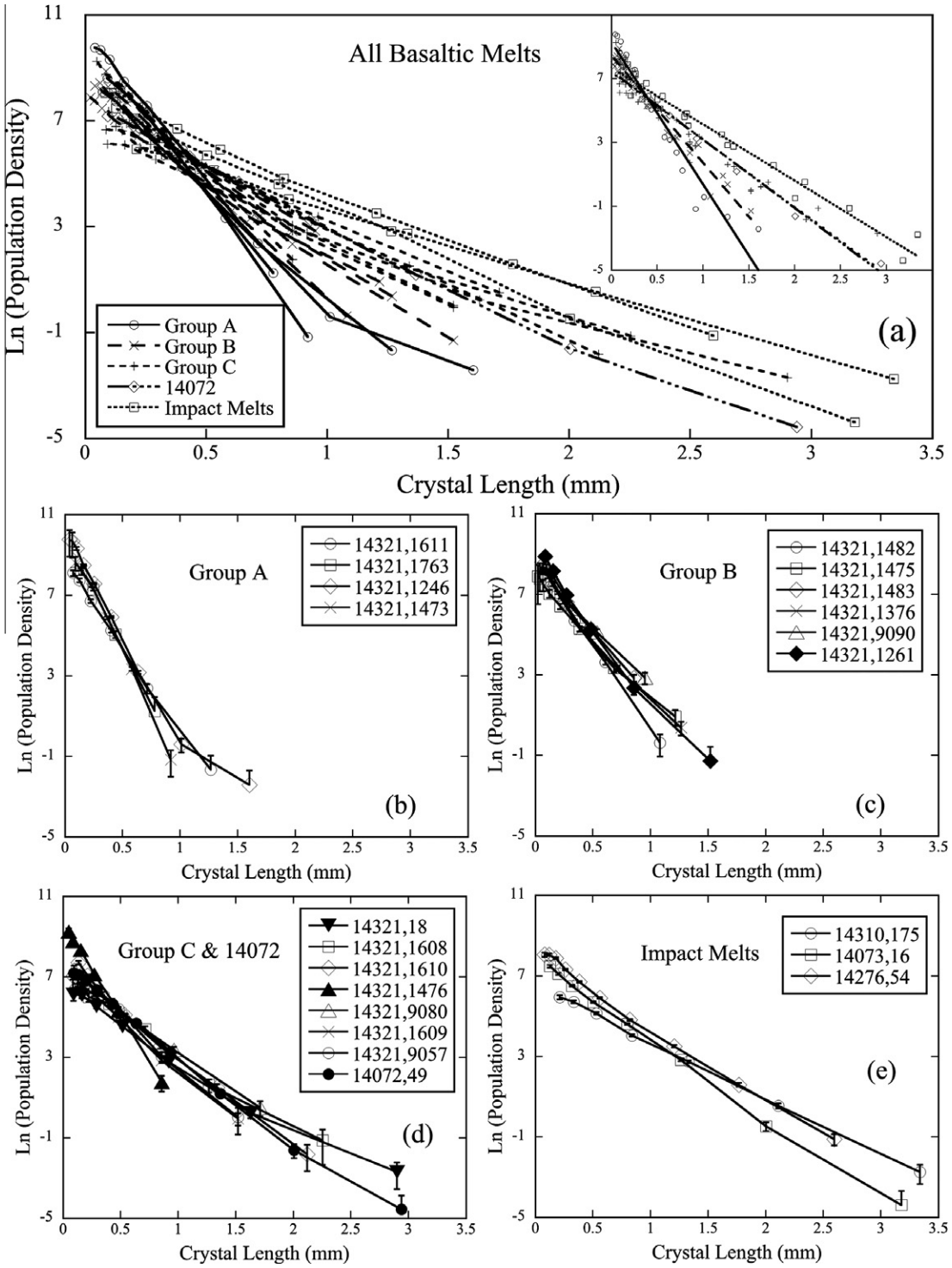

Fig. 3. CSDs of (a) all high-Al basaltic melts in this study, (b) Group A basalts, (c) Group B basalts, (d) Group C basalts and basalt 14072, and (e) the impact melts. The inset in (a) is the CSD plot of each sample group.

(Fig. 4a). The anorthite (An) mole percentages of Group A plagioclase crystals range from 84 to 96, Group B crystals range from 77 to 93, Group C crystals range from 84 to 96, 14072 crystals range from 73 to 93 and impact-melt crystals range from 64 to 95 (Fig. 4a). The values of the pristine basalt An% overlap with those measured by Shervais et al. (1985; $An_{77–96}$), Neal et al. (1988; $An_{69–97}$), Neal et al. (1989b; $An_{75–97}$), and Hagerty et al. (2005; $An_{89–93}$), though the range is more comparable to that in Neal et al. (1989b). FeO concentration and anorthite content of plagioclase are inversely correlated in all the samples studied here (Fig. 4b). Groups A, B and C basalts have

Table 2
Crystal size distribution data by group.

Group	Thin section	Crystal counted	Pl[b] vol.%	Slp1[c]	Int1[d]	Slp2[e]	Int2[f]	Slp1–Slp2[g]
A	14321.1473	596	9.18	−12.23	10.23	N/A	N/A	N/A
A	14321.1611	479	12.36	−9.05	8.83	−7.29	7.58	−1.76
A	14321.1763	1215	12.56	−11.13	9.92	N/A	N/A	N/A
A	14321.1246	2501	14.27	−10.70	10.26	−3.40	3.03	−7.30
B	14321.1376	686	20.44	−7.72	8.67	−5.31	7.10	−2.41
B	14321.1261	451	15.58	−8.15	9.26	−5.45	7.01	−2.70
B	14321.1475	211	22.91	−6.56	7.82	−4.53	6.44	−2.03
B	14321.1483	476	16.88	−6.58	8.45	N/A	N/A	N/A
B	14321.9090	202	17.80	−6.29	8.68	N/A	N/A	N/A
B	14321.1482	777	21.55	−8.40	8.69	−8.46	8.77	0.06
C	14321.9080	296	26.36	−4.56	7.67	−3.83	7.07	−0.73
C	14321.1476	547	14.99	−9.28	9.71	N/A	N/A	N/A
C	14321.9057	210	15.64	−5.68	7.97	−4.54	6.93	−1.14
C	14321.1610	1055	20.51	−5.77	8.30	−4.24	7.18	−1.53
C	14321.1608	173	16.71	−3.80	7.11	−2.79	5.16	−1.01
C	14321.18	464	29.74	−4.41	6.82	−2.31	4.00	−2.10
C	14321.1609	629	17.98	−5.42	7.54	−4.35	6.58	−1.07
14072	14072.49	3071	26.61	−4.86	7.77	−3.62	5.96	−1.24
IM[a]	14310.175	1368	32.55	−2.69	6.44	−2.73	6.35	0.04
IM[a]	14073.16	2810	37.10	−4.25	7.94	−3.73	7.34	−0.52
IM[a]	14276.54	4050	45.42	−4.69	8.59	−3.32	7.49	−1.37

[a] Impact melt.
[b] Plagioclase modal abundance obtained by using the area ratio of plagioclase and all the phases on the thin section.
[c] Slope measured from size intervals 0.1–1.0 mm.
[d] *y*-Intercept of slope 1.
[e] Slope measured from size intervals 1.0 mm to the largest. In the case that there is only one size interval >1.0 mm, the one closest to 1.0 mm was used in regression for slope2 and intercept2.
[f] *y*-Intercept of slope 2.
[g] A measure of CSD concavity.

similar trends in terms of the correlation between FeO concentration and anorthite content, but are distinctly different from 14072 and the impact melts (Fig. 4b).

The concentrations of trace elements in plagioclase grains with respective major-element concentrations for the different samples analyzed in this study are presented in the electronic annex (EA-1). Trace-element concentrations obtained in this study can have more than an order of magnitude difference within a plagioclase grain and between crystal grains in each group (EA-1), in contrast to relatively constant values obtained by Hagerty et al. (2005). In the pristine basalts the variation is almost two orders of magnitude, while in the impact melts the variation is less than an order of magnitude. There are no obvious correlations between trace-element ratio (e.g., La/Sr) and anorthite content in plagioclase of pristine basalts (Fig. 4c).

4. DISCUSSION

4.1. Textural analysis

Several petrologic processes can be inferred from CSDs. For example, if crystal nucleation and growth continue uninterrupted, a linear distribution of crystal sizes will be likely yielded (Marsh, 1988, 1998). Nonlinear CSDs may be produced by a variety of dynamic and kinetic processes and are indicative of changes in crystal nucleation and growth rates — such as crystal accumulation, magma mixing, or textural coarsening (i.e., growth of larger crystals at the expense of smaller ones) (e.g., Marsh, 1988; Higgins, 1996, 2011a; Higgins and Roberge, 2003).

Each group of pristine basalts (A, B, and C) and the impact melts are distinct in the CSD diagram (Fig. 3), and ungrouped sample 14072 falls within the Group C range (Fig. 3a). Although the CSDs within given groups appear similar, the CSD of 14321, 1426 is concave upward (Fig. 3b), which is consistent with textural coarsening occurred during magma crystallization (e.g., Marsh, 1998; Higgins, 2011b). The ranges of plagioclase grain sizes between samples are variable (Fig. 3 and Table 2). This makes it difficult to have a true sample-to-sample comparison. Therefore, only the slopes and the intercepts derived from the regressions of CSDs within the size intervals of 0.1–1 mm are discussed here because this size range encompasses every sample. The slope is determined using only those size bins that show an increasing population density with decreasing size, and from this slope the intercept is then calculated. It should be noted that the CSD slope and intercept are not independent of each other (Fig. 5a; Higgins, 2002; Zieg and Marsh, 2002) and no samples can lie above the closure limit in a CSD diagram (Higgins, 2002). Closure limits occur when volumetric phase proportions cannot exceed a certain percentage determined by the number of phases present in the rock, whose sum cannot exceed 100%. Therefore, because the CSD *y*-intercept represents the nucleation density of new crystals, as the magma

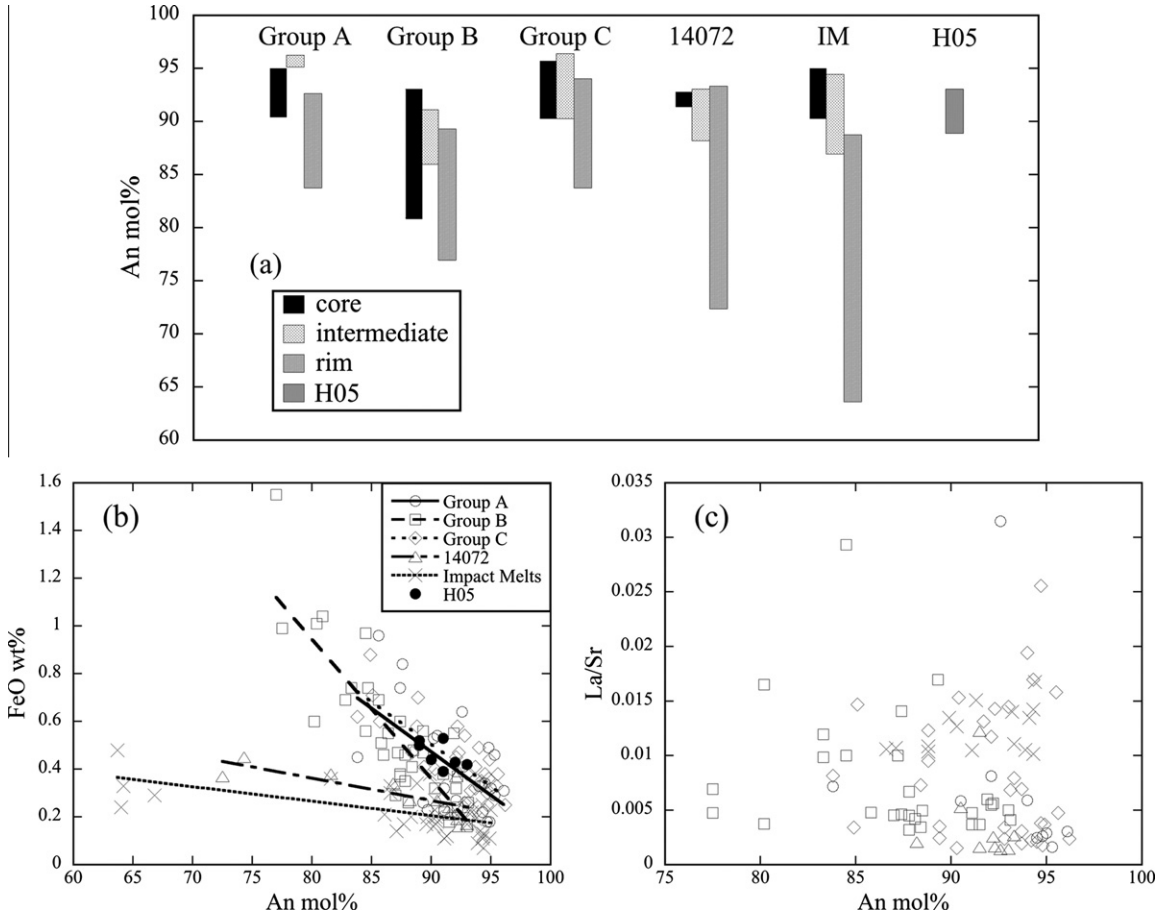

Fig. 4. (a) Ranges of anorthite content in plagioclase crystals analyzed in this study. (b) FeO concentration is generally correlated with anorthite content in plagioclase. (c) La/Sr in plagioclase crystals plotted against anorthite content. Data from Hagerty et al. (2005) are plotted (H05) for comparison.

approaches 100% crystallization, new crystals cannot form unless other crystals become smaller, thus increasing the slope through breakdown of the larger crystals. Conversely, textural coarsening causes a decrease in the CSD slope. At this point, any petrogenetic process that changes the slope of the CSD also changes the intercept (Higgins, 2002). Hence, a plot of plagioclase abundance versus characteristic length ($L_D = -1/\text{slope}$) is a more informative measure of CSD dispersion (Fig. 5b) as recommended by Higgins (2002). According to Eq. (1), the characteristic length is the product of the average crystal growth rate (G) and the average crystal residence time (τ) in the system. Fig. 5b shows that Group A and B basalts plot separately from each other and from Group C basalts (and impact melts), with the exception of one Group C basalt (14321, 1476), which is the only basalt separated from its respective group. Group C basalts exhibit the most variability (Fig. 5b), which is consistent with the whole-rock geochemical variability as shown by Neal and Kramer (2006). The impact melts have the highest volumetric plagioclase abundances, and also their characteristic lengths are among the longest (Fig. 5b), indicating that the impact melts crystallized relatively slowly compared to the pristine basalts. On the other hand, the intercepts of the different groups are not distinctly separated, which indicates that all melts had similar nucleation densities (Table 2, Fig. 5c). While the manifestation of textural groups could be due to the statistics of small numbers, the present data set suggests that the groups of high-Al basaltic melts defined by whole-rock geochemistry are also texturally distinct. There appears to be a geochemical and textural distinction between the pristine basalts and the impact melts (Fig. 5b; Neal and Kramer, 2006), although more impact melts will need to be analyzed in order to confirm this.

4.2. Petrogenetic modeling of Apollo 14 high-Al basaltic melts

4.2.1. Overview

Anorthite content and FeO concentration of plagioclase in the Apollo 14 samples studied here are generally correlated (Fig. 4b), which results from compositional evolution of the magma following a typical liquid line of descent. However, incompatible-trace-element ratios of plagioclase in these samples are not correlated with plagioclase anorthite content in pristine basalts (e.g., Fig. 4c). Whole-rock

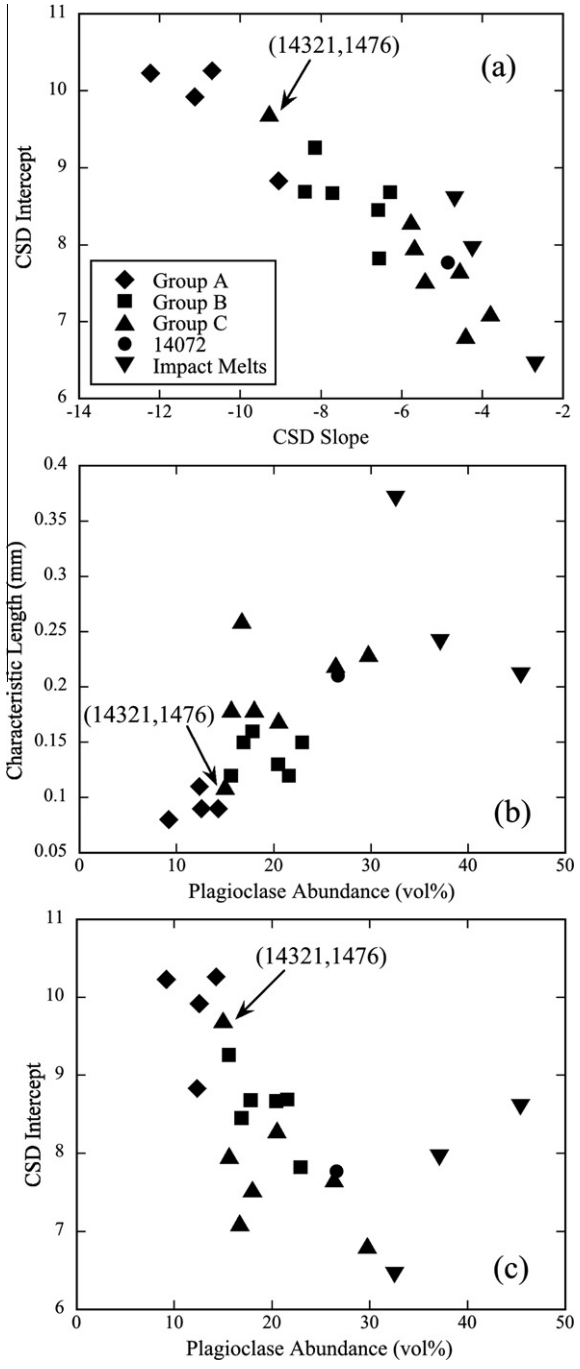

Fig. 5. (a) Correlation between the slopes and the intercepts of plagioclase CSDs. (b) Plagioclase characteristic length (L_D) as a function of modal abundance (volumetric percentage). (c) The intercepts as a function of plagioclase modal abundance. The slopes and intercepts of CSDs are regression results based on the size intervals from 0.1 to 1.0 mm. See text for discussion.

compositions of Apollo 14 high-Al basalts suggest that while Group A basalts could have formed by 30–40% closed-system fractional crystallization (FC), Group B and C basalts require assimilation of a distinct, evolved composition in conjunction with fractional crystallization (AFC) (Neal and Kramer, 2006, and references therein). The assimilants were a mixture of evolved components found at the Apollo 14 site: KREEP-rich QMG and granite (Table 3; Warren et al., 1983a; Jolliff, 1991; Neal and Kramer, 2006) due to the fact that there has been proposed a genetic relationship between KREEP and granite (e.g., Ryder, 1976; Neal and Taylor, 1991).

Using the plagioclase trace-element data, modeling of fractional crystallization and assimilation scenarios were carried out to test the petrogenetic models described by Neal and Kramer (2006), where plagioclase becomes a liquidus phase after >20% crystallization. The estimated parental melt compositions (Table 4; Neal and Kramer, 2006) were used to calculate the Rayleigh fractional crystallization (FC) trajectories for each basalt group and the impact melts. Assuming that there was no significant crystal accumulation (an assumption supported by petrographic observations), the hybrid parent compositions were estimated by taking the lowest value for each incompatible trace element within a database of all basalt compositions of each group (Neal and Kramer, 2006). The fraction of residual melt and trace-element bulk partition coefficients between solid phase and the residual melt change during magma evolution to reflect the changing melt composition, phase assembly and melt fraction, respectively, as described by the crystallization sequence and modeling results of Neal and Kramer (2006). This fractional crystallization trajectory was compared to the elemental concentrations of the equilibrium melt from which each sample spot on the plagioclase crystals formed using the equation:

$$C_i^{\mathrm{m}} = C_i^{\mathrm{plag}} / D_i^{\mathrm{plag}}, \tag{2}$$

where D_i^{plag} is the partition coefficient of element i between a plagioclase crystal and the residual melt, and depends on the anorthite content of the plagioclase (e.g., Blundy and Wood, 1991; Bindeman et al., 1998; Tepley et al., 2010; see below), C_i^{plag} and C_i^{m} are the weight concentration of element i in the plagioclase and the melt respectively. Similarly, the AFC trajectory was calculated using the following AFC modeling equation (DePaolo, 1981):

$$\frac{C_i^{\mathrm{m}}}{C_i^0} = F^{-z_i} + \left(\frac{r}{r-1}\right)\frac{C_i^{\mathrm{a}}}{z_i C_i^0}\left(1 - F^{-z_i}\right), \tag{3}$$

where C_i^0 and C_i^{a} are the weight concentration of element i in the parental melt and assimilated component respectively, F is the fraction of melt remaining, $z_i = (r + D_i - 1)/(r - 1)$, and D_i is the bulk partition coefficient of element i between crystallizing phases and the residual melt.

4.2.2. Partition coefficients and equilibrium melts

The uncertainty in partition coefficient determinations can be a major source of error in modeling magmatic processes using mineral chemistry (e.g., Blundy, 1997; Bédard, 2001). To deduce the processes that occurred during the magma evolution of each Apollo 14 high-Al basaltic melt, partition coefficients have to be estimated carefully so that the calculated trace-element concentrations in the melts that equilibrated with plagioclase crystals (Eq. 2) are as realistic as possible. Numerous studies have been carried out to determine the partition coefficients for trace elements

Table 3
Assimilant compositions (in ppm) used in the modeling of each basalt group.

	Group A assimilant	Group B assimilant	Group C assimilant	14072 Assimilant	QMG[a]		Granite[a]	
					14161.7069	14161.7373	14303.204	14321.1027
Sr	86	65	90	165	160	207	210	55
Y[b]	7900	1650	994	4250	798.4	994	204	201
Ba	790	740	760	2100	2050	740	2100	2160
La	135	125	119	185	228	696	58	44.3
Ce	1225	250	250	710	537	1683	149	117
Sm	326	50	45	320	97	326	22	15.9
Eu	1.5	1.3	2	5.6	3.35	5.68	3.3	1.17
Props B[c] (%)					30	30	20	20
Props C[c] (%)					40	0	10	50

[a] Data sources: QMG: Jolliff (1991). Granite: Warren et al. (1983a).
[b] Yttrium concentrations in QMG and granite estimated by Neal and Kramer (2006).
[c] Proportions of QMG and granite as assimilant of Group B and C basalts based on the whole-rock data (Neal and Kramer, 2006).

Table 4
Parental melt compositions (in ppm) used in the modeling of each basalt group and the impact melts.

	Group A[a]	Group B[a]	Group C[a]	Basalt 14072	Impact melt
Sr	56	85	56.5	92.4	165
Y	20.1	62.5	28.3	36	174
Ba	30.6	120	54	103	515
La	2.62	17	5.4	6.8	56
Ce	7.31	46	15.1	19.2	143
Sm	1.6	8.74	3.28	4.05	21
Eu	0.52	1.11	0.52	0.92	1.9

[a] Parental melt compositions of Groups A, B, and C basalts determined by Neal and Kramer (2006).

Table 5
Partition coefficients of trace elements used to calculate equilibrium melt compositions.

	a[a]	b[a]	Range of values[b]	Literature value[c]
Ga	–	–	0.94	–
Sr	−274.25	26509	1.010–1.536	1.61
Y	−932.31	18998	0.003–0.013	0.027
Ba	−386.05	10058	0.110–0.198	0.686
La	−791.39	27736	0.019–0.064	0.042
Ce	−657.19	14606	0.019–0.052	0.047
Sm	−908.66	29062	0.009–0.034	0.017
Nd	−775.84	22492	0.014–0.046	–
Eu	–	–	0.698	1.2
Er	−1611.8	72825	0.0012–0.014	–
Yb	−3416.6	219566	0.0001–0.025	0.007

[a] a and b are fitting parameters of Eq. (4) for each element. The regressions are shown in Fig. 6.
[b] The ranges of partition coefficients used to calculate equilibrium melt compositions. These values were calculated using Eq. (4) with the parameters in left two columns at 1473 K. See text for discussion of partition coefficients of Eu and Ga.
[c] The partition coefficients used for modeling mare basalt petrogenesis in Snyder et al. (1992) and Neal and Kramer (2006).

between plagioclase and melt under different conditions (see Bédard, 2006, and references therein). The dependence of D_i^{plag} on anorthite content of plagioclase has been experimentally verified as (e.g., Blundy and Wood, 1991; Bindeman et al., 1998; Bédard, 2006; Tepley et al., 2010):

$$RT \ln D_i^{plag} = a_i X_{An} + b_i, \quad (4)$$

where X_{An} is the anorthite mole percentage in plagioclase, R is the gas constant, T is temperature in K, a_i and b_i are fitting parameters for element i. Furthermore, the trace-element concentrations in the melt can also affect their partition coefficients (Bindeman et al., 1998; Bindeman and Davis, 2000), which makes it problematic to use partition coefficients determined from doped experimental charges in modeling magmatic processes.

Partition coefficients for Sr, Y, Ba, La, Ce, Nd, Sm, Er, and Yb for plagioclases in the current study (X_{An} = 77–96, see EA-1) were calculated using Eq. (4) with parameters a and b listed in Table 5. The values of a and b for these elements were achieved by fitting Eq. (4) to literature data

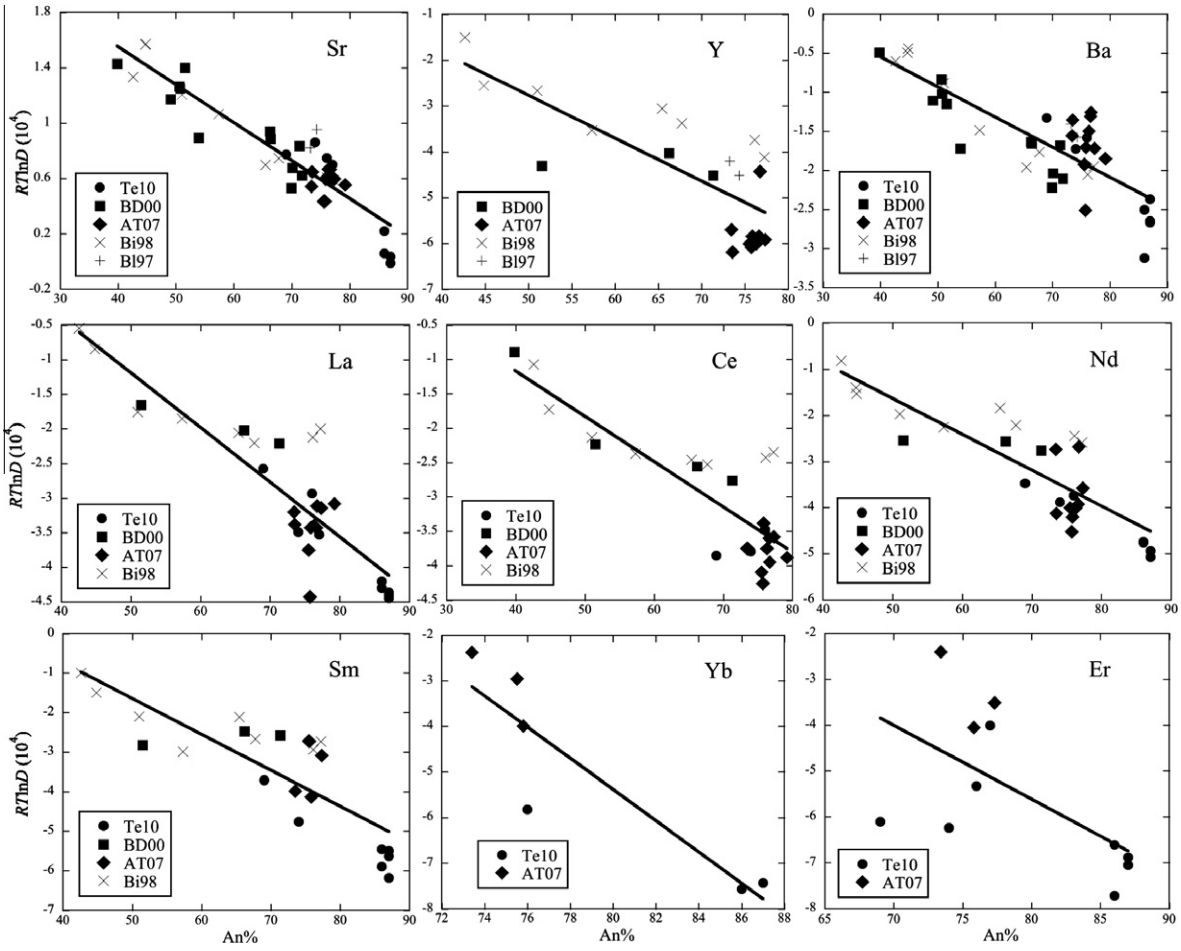

Fig. 6. $RT\ln D_i^{plag}$ (i = Sr, Y, Ba, La, Ce, Nd, Sm, Er and Yb) plotted against plagioclase anorthite content. The data sources: Te10 (Tepley et al., 2010), BD00 (Bindeman and Davis, 2000), AT07 (Aigner-Torres et al., 2007), Bi98 (Bindeman et al., 1998), and Bl97 (Blundy, 1997). The solid line is the regression of Eq. (4) and the fitting results are listed in Table 5.

(Blundy, 1997; Bindeman et al., 1998; Bindeman and Davis, 2000; Aigner-Torres et al., 2007; Tepley et al., 2010) (Fig. 6). The data selection criteria are: (1) The trace-element concentrations in sample charges should be at the natural level (i.e., not doped with excess levels of the trace element); (2) Only the data from the experiments carried out under 1 bar pressure with nominally anhydrous samples are included as we assume near or at the surface crystallization for these basalts; (3) The trace-element concentrations of the melts and plagioclase crystals in the experimental charges were measured by SIMS or LA-ICP-MS; (4) The data in a synthetic albite-anorthite-diopside system (Bindeman et al., 1998) are inconsistent with those from natural systems and are excluded.

Europium plagioclase/melt partition coefficient exhibits strong dependence on oxygen fugacity (e.g., Weill and McKay, 1975; Aigner-Torres et al., 2007). The oxygen fugacity during lunar basalt crystallization is generally at or below IW buffer (e.g., Sato et al., 1973; Haggerty, 1978; Papike and Bence, 1978; Anand et al., 2006), which is different from the terrestrial atmospheric condition at which most partition experiments were carried out (e.g., Bindeman et al., 1998). Only a few studies were conducted at IW buffer or below (Weill and McKay, 1975; McKay and Weill, 1977; Aigner-Torres et al., 2007). The experimental charges in Weill and McKay (1975) and McKay and Weill (1977) were doped with high-concentrations of REE. Hence only the data in Aigner-Torres et al. (2007) fall in the selection criteria. An average value ($D_{Eu}^{plag} = 0.698$) of three data points at 1473 ± 20 K and IW buffer in Aigner-Torres et al. (2007) was used in modeling petrogenesis of the Apollo 14 high-Al basaltic melts. No experimental data are available for partition coefficient of Ga with our selection criteria. Hence an average value ($D_{Ga}^{plag} = 0.94$) of the partition coefficients deduced from natural terrestrial plagioclase crystals An_{75-92} (Goodman, 1972) was used in our modeling. These Ga partition coefficients obtained from natural samples have also been used in other lunar studies (e.g., Warren and Kallemeyn, 1984), but should be viewed with caution.

Fig. 7 shows comparisons of calculated trace-element concentrations in melts equilibrated with plagioclase crystals using the D_i^{plag} (Table 5) and whole-rock compositions from Neal and Kramer (2006). In general, the residual melts became enriched in incompatible trace elements as melt crystallization continued (Fig. 7). But assimilation of

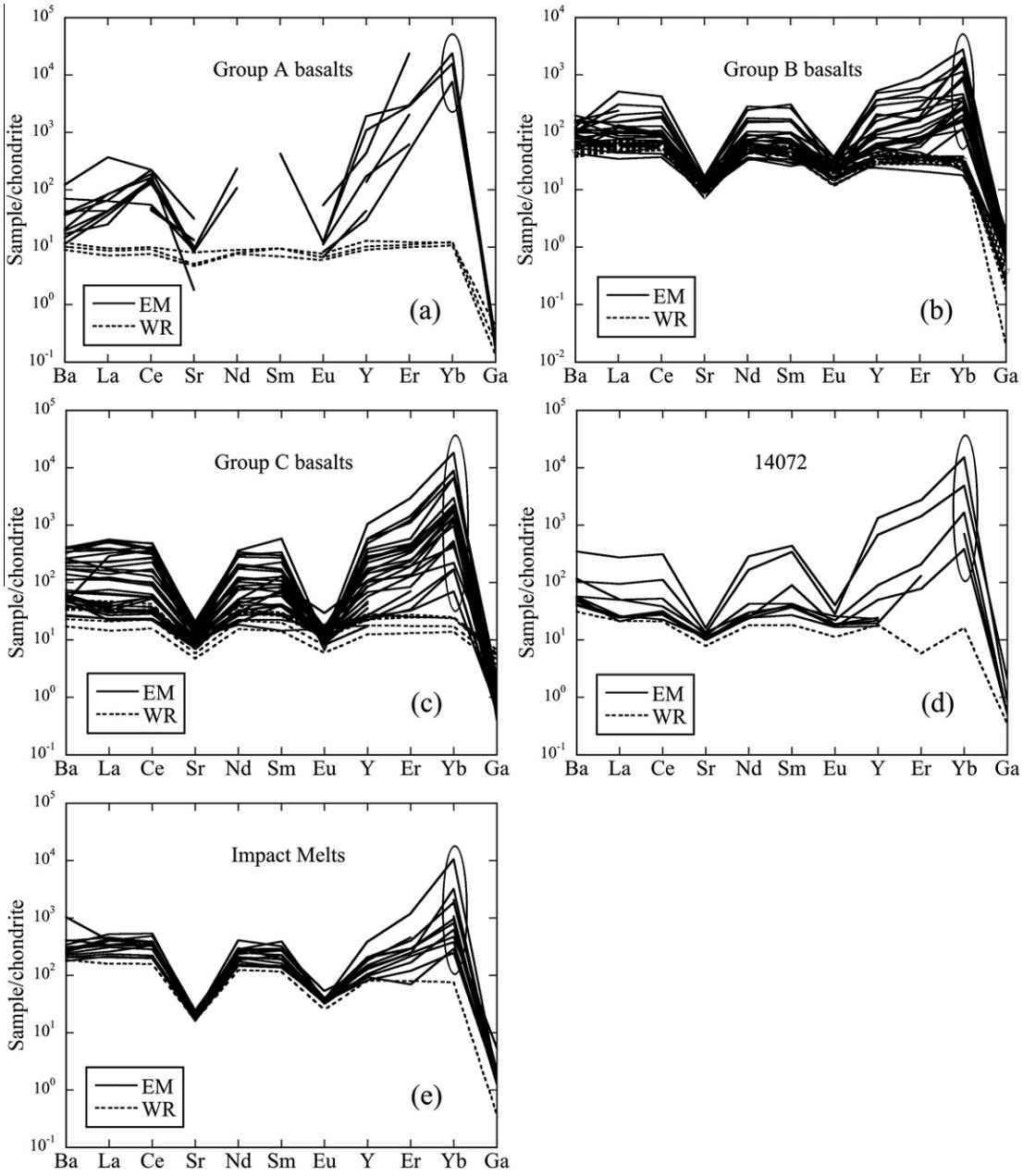

Fig. 7. Calculated trace-element profiles of melts equilibrated with plagioclase grains in (a) Group A, (b) Group B, and (c) Group C basalt, (d) basalt 14072 and (e) the impact melts. Whole-rock profiles from Neal and Kramer (2006) are also included (dashed lines). The calculated high values of Yb in equilibrium melts highlighted by an ellipse may be caused by underestimated partition coefficients using Eq. (4) due to lack of experimental constraints (Fig. 6). EM: composition of melt equilibrated with plagioclase, WR: whole-rock composition.

an incompatible-trace-element-rich component can bolster this enrichment in the residual melts (see Section 4.3). Strontium and Eu show negative anomalies in the residual melts (Fig. 7) mostly because Sr and Eu are less incompatible than other trace elements in plagioclase (Table 5). The composition of the assimilant also contributes to these anomalies.

Bulk partition coefficients of trace elements between solid phase and the residual melt are important parameters in calculating FC and AFC trajectories (e.g., Neal and Kramer, 2006). During magma evolution, bulk partition coefficients depend on not only the modal abundances of the crystallizing phases, but also the chemical compositions of the individual phases (such as plagioclase) and the residual melt, which control the trace-element partition coefficients between the individual phases and the residual melt. To simplify our calculations, we considered the effect of modal abundances of the crystallized phases and plagioclase chemical composition in each stage on bulk partition coefficients, the same as the approach in the previous studies (e.g., Hagerty et al., 2005; Neal and Kramer, 2006). The partition coefficients between other mineral phases and the

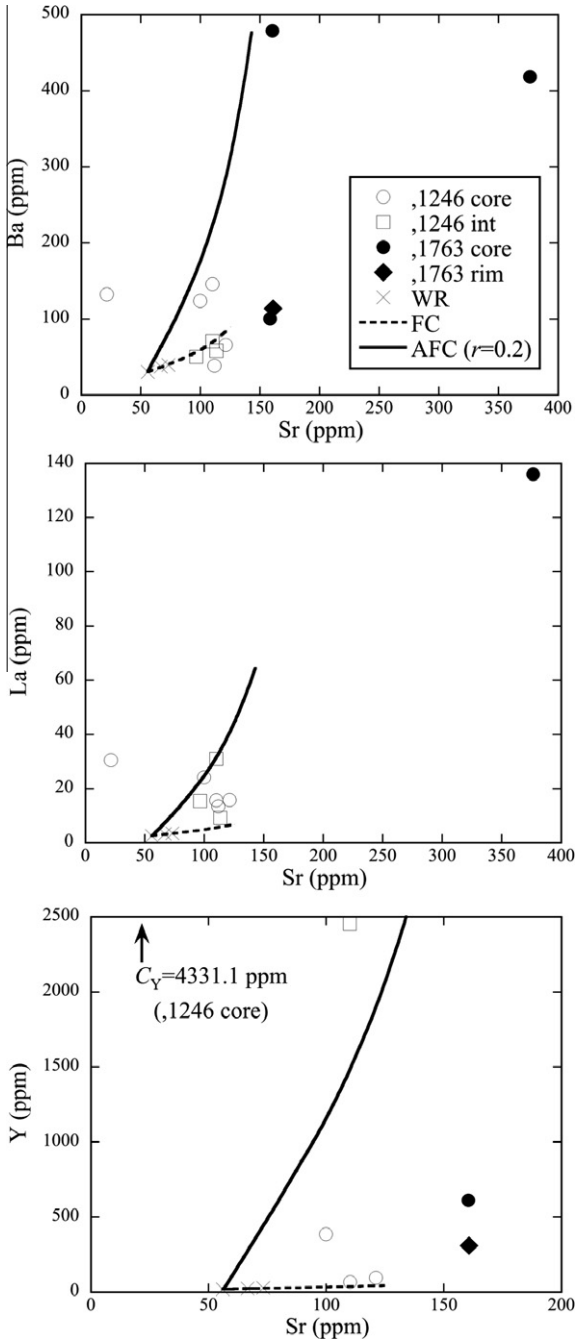

Fig. 8. Ba, La, and Y plotted against Sr for Group A basalts. Also shown are the FC and AFC with an *r*-value (r = mass assimilated/mass crystallized; DePaolo, 1981) trajectories from the parent (Neal and Kramer, 2006) to 99% total crystallization, and whole-rock (WR) data (Neal and Kramer, 2006). Modeling parameters are given in Tables 3–6.

melt used in FC and AFC calculations were: apatite, the experimental values in Prowatke and Klemme (2006); olivine, spinel, orthopyroxene, pigeonite and augite, the literature data used in Neal and Kramer (2006). In all modeling presented below, FC and AFC trends were calculated to 99% crystallization.

4.2.3. Petrogenetic modeling of Group A basalts

Whole-rock trace-element data suggested that the Group A basalts were produced by 30–40% closed-system FC (Neal and Kramer, 2006). The equilibrium-melt conditions recorded by the plagioclase crystals suggest otherwise. The parental melt composition for Group A basalts (Table 4) from Neal and Kramer (2006) was used. Unlike the whole-rock data, the trace-element composition in equilibrium melts indicates that small amounts of assimilation also occurred at the end of melt evolution. As such, the assimilation is not indicated in the whole-rock trace-element data (Neal and Kramer, 2006). The solid lines in Fig. 8 represent the model of AFC with an *r*-value (r = mass assimilated/mass crystallized; DePaolo, 1981) of 0.2 and a mixed KREEP-granite assimilant composition defined in Table 3.

4.2.4. Petrogenetic modeling of Group B basalts

The petrogenesis of Group B basalts was modeled based on the parental composition (Table 4) and seven-stage crystallization sequence (Table 6) established in Neal and Kramer (2006). Modeling of the Group B basalts used a mixed KREEP-granite assimilant (Table 3), D_i^{plag} (Table 5) and a variable *r*-value to best fit the plagioclase-equilibrium-melt compositional arrays (Fig. 9).

Most plagioclase equilibrium melt compositions fall between the FC trajectory and the AFC trajectory with an *r*-value of 0.5 (Fig. 9). If the *r*-value fluctuated during the petrogenesis of the Group B basalts and diffusion did not homogenize the trace element distribution in the melt, then the equilibrium melt compositions calculated from different locations on plagioclase crystals would not fall on a single AFC trajectory (Fig. 9); whole-rock trace-element compositions, on the other hand, would suggest an AFC trajectory with an *r*-value representing the weighted average of all *r*-values experienced during petrogenesis. This discrepancy is seen in Fig. 9, where the bulk of the equilibrium melt compositions fall in the region outlined by the AFC trajectory ($r = 0.5$) and the FC trajectory. It is also possible that the assimilant composition was not constant during the basalt crystallization and diffusion in the magma was not fast enough to homogenize the trace element distributions in the residual melt (Table 3), which would also cause disparities between the whole-rock model of Neal and Kramer (2006) and that developed here.

4.2.5. Petrogenetic modeling of Group C basalts

The petrogenesis of Group C basalts was modeled using the parental melt composition (Table 4) and crystallization sequence (Table 6) established in Neal and Kramer (2006). A mixed KREEP-granite assimilant was used, but one of different composition to that for the Group B modeling (Table 3). Partition coefficients used were deduced from the rationale outlined in Section 4.2.2 (Table 5), and the *r*-value was varied so that the data were encompassed by model pathways as shown in Fig. 10, which shows the FC and AFC trajectories compared to the equilibrium-melt concentrations on trace-element plots for the Group C basalts. Most of the plagioclase-equilibrium-melt compositions fall in the region between the AFC trajectory (with an *r*-value of 0.5) and the FC trajectory (Fig. 10). The fact that all

Table 6
Crystallization sequence of Groups A, B and C basalt, 14072 and the impact melts.

Group A[a]	Stage	1	2	3	4	5	6	7	8	Projection 1	Projection 2
	Total cryst.	1%	5%	10%	14%	24%	28%	32%	44%	75%	99%
Olivine (%)	92	95	82	30	30						
Spinel (%)	8	5	3								
Plagioclase (%)						10	10	10	25	45	
Orthopyroxene (%)			15	40	36						
Augite (%)						32	65	65	65	55	
Pigeonite (%)				30	34	58	25	25	10		
Apatite (%)										5	

Group B[a]	Stage	1	2	3	4	5	6	7	Projection 1	Projection 2	Projection 3
	Total cryst.	1%	5%	10%	15%	20%	25%	37%	57%	77%	99%
Olivine (%)	95	50	82	30	30						
Spinel (%)	5	4	3								
Plagioclase (%)						10	10	20	25	30	
Orthopyroxene (%)		46	15	40	36						
Augite (%)						32	65	60	55	50	
Pigeonite (%)				30	34	58	25	20	20	20	

Group C[a]	Stage	1	2	3	4	5	6	7	Projection 1	Projection 2	Projection 3
	Total cryst.	1%	4%	9%	13%	17%	22%	32%	46%	66%	99%
Olivine (%)	90	95.6	86.5	60	30						
Spinel (%)	10	4.4	3.5								
Plagioclase (%)								20	25	15	
Orthopyroxene (%)			10	40	36						
Augite (%)						32	65	60	50	60	
Pigeonite (%)					34	68	35	20	25	25	

Basalt 14072[b]	Stage	1	2	3	4	5	6	7	Projection 1	Projection 2	Projection 3
	Total cryst.	1%	4%	9%	13%	17%	22%	32%	46%	66%	99%
Olivine (%)	55	60	30	20	10						
Spinel (%)	45	40	40								
Plagioclase (%)						10	20	30	55	45	
Orthopyroxene (%)			30	40	35	20	10				
Augite (%)						30	40	50	40	55	
Pigeonite (%)				40	55	40	30	20	5		

Impact melt[b]	Stage	1	2	3	4	5	6	7	8	Projection 1	Projection 2
	Total cryst.	1%	5%	10%	14%	24%	28%	32%	44%	75%	99%
Olivine (%)	50										
Spinel (%)	40	20	10								
Plagioclase (%)	10	10	20	20	20	20	30	60	70	75	
Orthopyroxene (%)		70	60	60	40	40	30				
Augite (%)				10	20	30	30	30	10	8	
Pigeonite (%)			10	10	20	10	10	10	19	15	
Apatite (%)									1	2	

[a] Stages for Groups A (1–8), B (1–7), and C (1–7) determined by Neal and Kramer (2006).
[b] Stages for 14072 and the impact melts determined with petrographic observations and *MELTS* simulation (Ghiorso and Sack, 1995).

equilibrium-melt compositions do not fall on a single FC or AFC trajectory suggests that, as with the Group B basalts, the either *r*-value fluctuated during crystallization and diffusion in the melt did not homogenize the trace element distributions, and/or the assimilant composition was not constant.

4.2.6. Petrogenetic modeling of basalt 14072

Basalt 14072 is a pristine, but ungrouped basalt (Neal and Kramer, 2006). The crystallization of 14072 was modeled using its whole-rock composition (Helmke et al., 1972; Taylor et al., 1972; Neal and Kramer, 2006) and calculated plagioclase-equilibrium-melt compositions (Fig. 7). The parental melt and assimilant compositions in the model are listed in Tables 4 and 3, respectively. As with the Groups A, B, and C basalts, the plagioclase-equilibrium-liquid compositions of basalt 14072 cannot be explained by just closed-system fractional crystallization process or an AFC trajectory of a constant *r* value. As with the other basalt groups, the petrogenetic model (Table 6, Fig. 11) suggests that 14072 evolved through an AFC process with a fluctuating *r*-value. Similarly, the assimilant composition may also have varied between components of KREEP and granite as the 14072 melt crystallized.

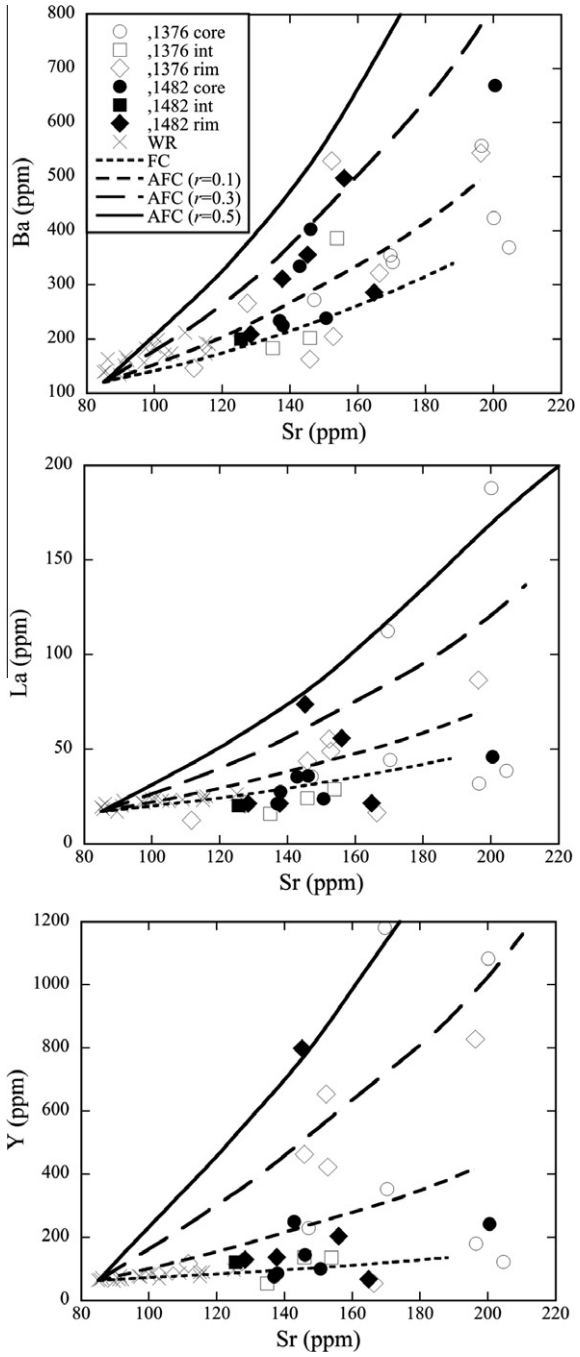

Fig. 9. Ba, La, and Y plotted against Sr for Group B basalts. Also shown are the FC and AFC trajectories from the parent (Neal and Kramer, 2006) to 99% total crystallization, and whole-rock (WR) data (Neal and Kramer, 2006). Modeling parameters are given in Tables 3–6.

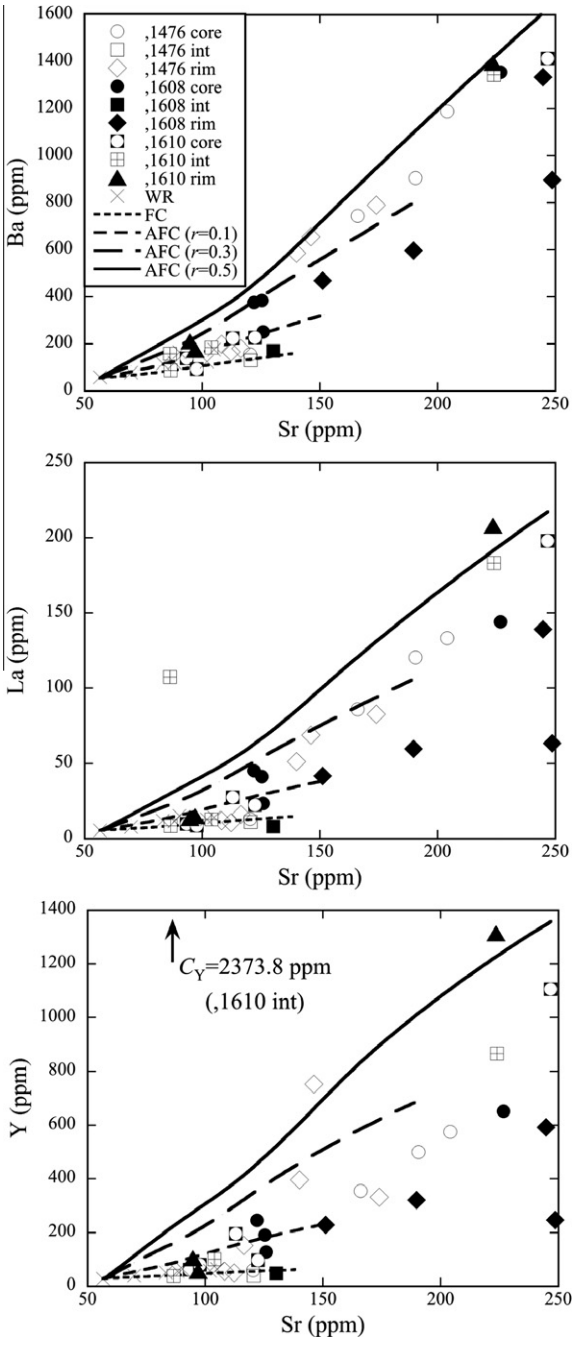

Fig. 10. Ba, La, and Y plotted against Sr for Group C basalts. Also shown are the FC and AFC trajectories from the parent (Neal and Kramer, 2006) to 99% total crystallization, and whole-rock (WR) data (Neal and Kramer, 2006). Modeling parameters are given in Tables 3–6.

4.2.7. Petrogenetic modeling of impact melts

The petrogenesis of impact melts 14073, 14276 and 14310 was modeled using a parental melt composition and crystallization sequence given in Tables 4 and 6, respectively. In contrast to the pristine basalts, the calculated plagioclase-equilibrium-melt compositions in the impact melts can be explained by closed-system fractional crystallization (Fig. 12). This is consistent with the previous petrological studies (e.g., Ridley et al., 1972). The whole-rock data of the impact melts 14310 (Brunfelt et al., 1972; Helmke et al., 1972; Hubbard et al., 1972; Masuda et al., 1972; Philpotts et al., 1972; Rose et al., 1972; Taylor et al., 1972; Willis et al., 1972; Neal and Kramer, 2006) and 14276 (Brunfelt et al., 1972; Rose et al., 1972) also fall on the trajectory of fractional crystallization (Fig. 12).

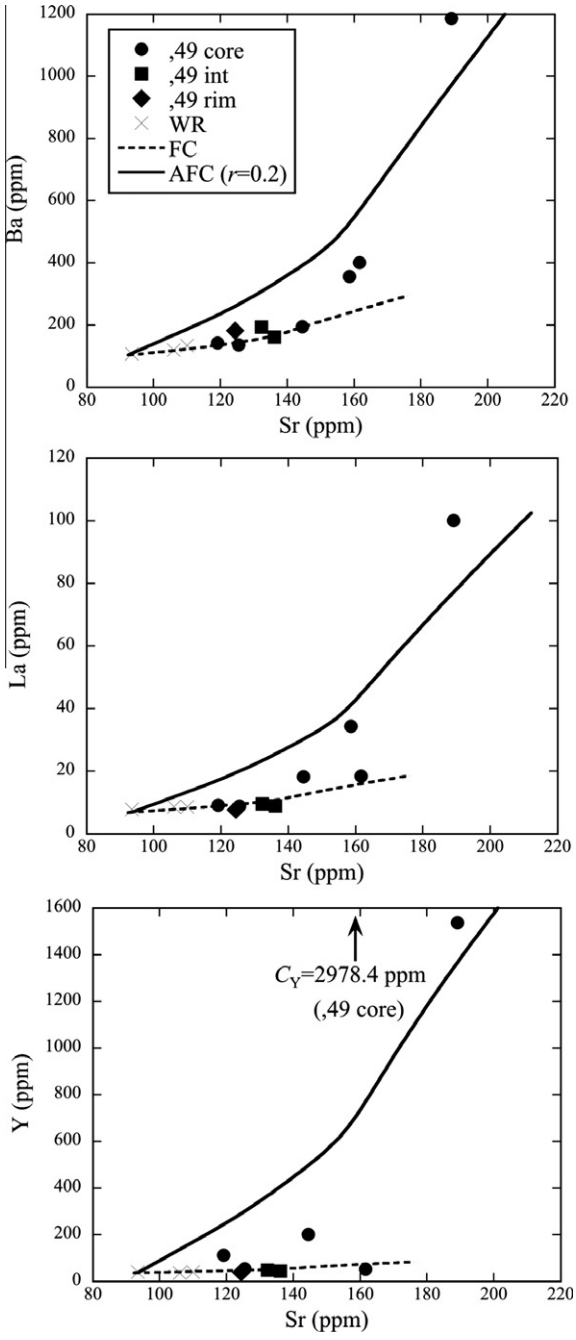

Fig. 11. Ba, La, and Y plotted against Sr for high-Al mare basalt 14072. Also shown are the FC and AFC trajectories from the parent to 99% total crystallization, and whole-rock (WR) composition (Helmke et al., 1972; Taylor et al., 1972; Neal and Kramer, 2006). Modeling parameters are given in Tables 3–6.

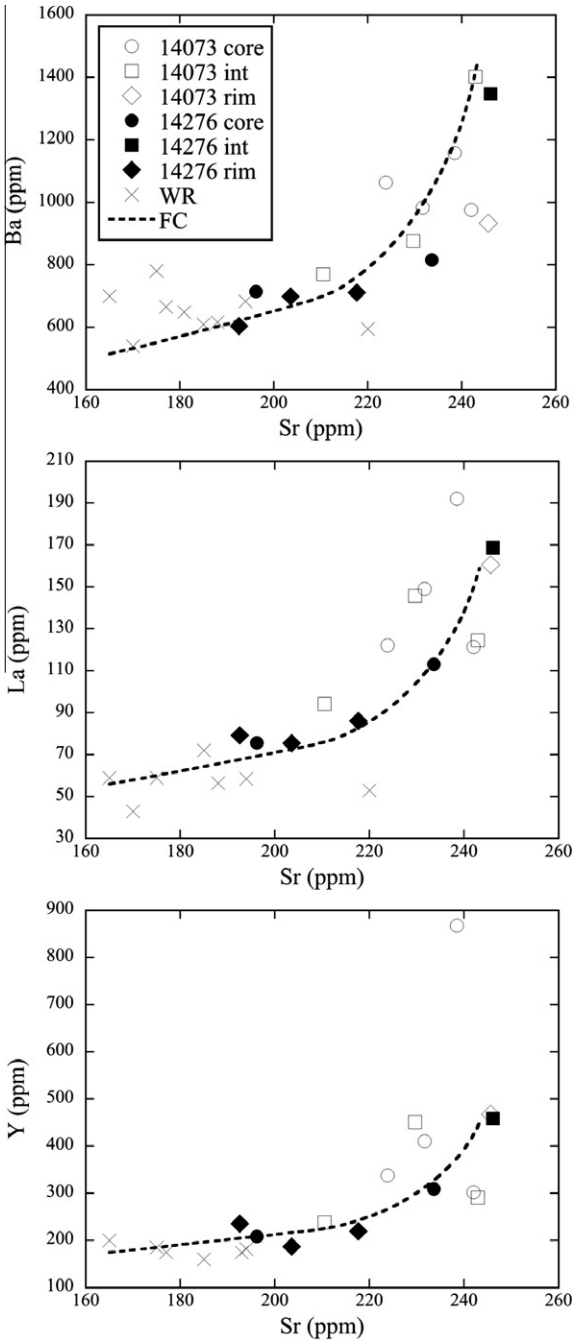

Fig. 12. Ba, La, and Y plotted against Sr for aluminous impact melts 14073 and 14276. Also shown is the FC trajectory from the parent to 99% total crystallization. The whole-rock data of 14276 and 14310 (see the text for the data source) are also plotted. Modeling parameters are given in Tables 4–6.

4.3. Geologic setting: pristine basalts versus impact melts

The compositional micro-heterogeneity in the pristine Apollo 14 high-Al basalts observed in this study suggests that these melts continued to evolve through open-system processes, possibly as they flowed across the lunar surface. The crystal stratigraphy derived from plagioclase crystals records open-system evolution in all basalt groups, including 14072. In looking at the modeling trajectories for the Groups A, B, and C basalts (Figs. 8–10), some of the plagioclase-equilibrium-melt compositions can be modeled by fractional crystallization, with some crystals requiring AFC with variable r values. We suggest that one way these variations resulted from assimilation and crystallization while the lava flowed across the lunar surface (e.g.,

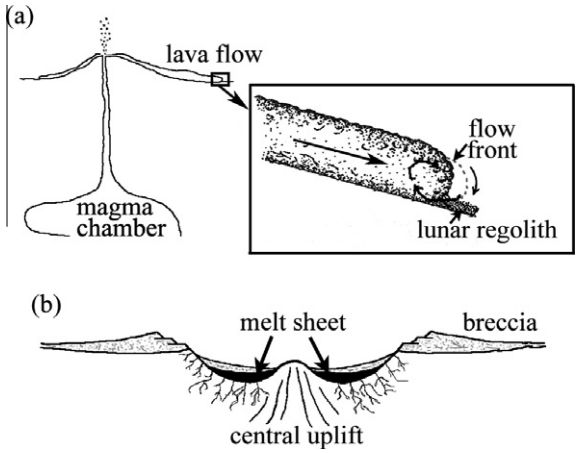

Fig. 13. Cartoons of geologic settings of basaltic melts: (a) basaltic lava erupted and flowing across the lunar surface (gradient is exaggerated) and how regolith material could have been incorporated and assimilated into the flow front; and (b) melts formed and ponding within the impact crater that do not flow, thus facilitating a slower cooling rate.

Crisp and Baloga, 1994; Keszthelyi and Self, 1998; Griffiths, 2000) as it incorporated low melting point components from the Procellarum KREEP Terrane (PKT). This has been observed on both Earth (e.g., Lesher and Campbell, 1993; Kauahikaua et al., 1998) and the Moon (e.g., Hulme, 1982). We propose that the pristine high-Al basalts crystallized in lava flows that had open channels connecting the vents to the flow fronts after their emplacement on the lunar surface (Fig. 13a). As the lava flowed across the surface, thermal erosion of the underlying regolith could occur with low-melting-point components, such as KREEP-rich and granite clasts, being preferentially assimilated (Fig. 13a). Heterogeneous distribution of these KREEP- and granite-rich materials would have promoted the fluctuating "*r*-values" we see from the modeling. Our modeling also suggests that assimilation did not occur at the onset of crystallization, but towards the end. Therefore, *r*-values of 0.5 would not dramatically affect the major element composition of the whole rock. It is assumed that the regolith at the time of lava effusion in the PKT was enriched in KREEP/granite-rich clasts. As this would be heterogeneously distributed in the surface regolith, the assimilant would have changed in terms of both composition (proportion of KREEP versus granite) and mass assimilated (*r*-value) throughout magma crystallization and within individual flows. Furthermore, trace elements in assimilated regolith were not in equilibrium with the melt composition completely. The re-equilibration process through diffusion would have been at least partially controlled by melt cooling rate. If the late crystallization stages of the Apollo 14 high-Al lavas were dominated by disequilibrium processes, this could explain data that plot beyond the 99% crystallization model curves (e.g., Fig. 9). However, a weighted average of all the assimilants for each group of high-Al basalts are the same as that obtained from whole-rock trace-element data (Table 3; Neal and Kramer, 2006). The much lower viscosity of lunar basaltic melts compared to terrestrial basalts (Murase and McBirney, 1970) can enhance both lava flow distance and entrainment rates of the material into the fluid center of the lava flow (e.g., Keszthelyi and Self, 1998). The assimilation of regolith by basaltic lava on the lunar surface has also been suggested for the petrogenesis of Apollo 12 ilmenite basalts where pleonaste spinels are suggested to be refractory xenocrysts after incorporation of the regolith as the lava flowed across the lunar surface (e.g., Dungan and Brown, 1977). One potential drawback for the surface assimilation model is the apparent lack of refractory xenocrysts in the Apollo 14 pristine basalts. However, the small size of the clasts may preclude the inclusion of any such xenocrysts in the thin section. Another potential drawback is that assimilation of regolith can potentially elevate the siderophile element contents of the magma, especially if the regolith contains remnant meteoritic metal. Again, the small sample size of the 14321 clasts that we studied here has precluded determination of the highly siderophile elements and while the nickel abundances of impact melts are generally higher (~100–500 ppm) than in the pristine basalts, the ranges of Ni abundances in the pristine basalts (~10–120 ppm) overlap the lower end of the impact melt range. Therefore, while it is certainly possible that meteoritic material could have been incorporated into the pristine high-Al basalts, we do not have any evidence in our samples that this has occurred.

In contrast to the pristine basalts, the petrogenetic modeling of the Apollo 14 aluminous impact melts shows the plagioclase formed through closed-system fractional crystallization (Fig. 12). It could be that the impact melts did not flow very far, thus reducing the opportunity of entraining and assimilating regolith with distinct components, that the pristine basalts were hotter than the impact-generated melts, and/or that the Apollo 14 aluminous impact melts were derived from an impact melt sheet that formed within the impact crater with no opportunity to interact with the low-melting-point evolved lithologies (Fig. 13b). The last scenario proposed for the aluminous impact melts was observed within an impact crater on Earth (e.g., O'Connell-Cooper and Spray, 2011). If the impact melts ponded within the crater, slower cooling (as shown by CSDs) of impact melts (Fig. 3) would be facilitated and assimilation of low-melting-point components as the melt flowed across the surface would not have occurred. The geologic scenarios of the Apollo 14 high-Al pristine melts inferred from plagioclase crystal stratigraphy suggest that AFC processes may have only occurred when the magma flowed across the surface. This is an abrupt departure from the conclusions drawn from the whole-rock modeling (e.g., Neal et al., 1988, 1989a; Neal and Taylor, 1990; Neal and Kramer, 2006).

4.4. CSDs and trace-element distributions: two prongs of the crystal stratigraphy approach

The crystal stratigraphy of plagioclase shows that Apollo 14 pristine high-Al basalts (Groups A, B and C basalt, and 14072) each exhibit a degree of assimilation during magma evolution (Figs. 8–11). Whole-rock trace-element data are consistent with this, except for Group A basalts where they suggest closed-system crystal fractionation (Neal and Kramer, 2006). The higher cooling rate of Group

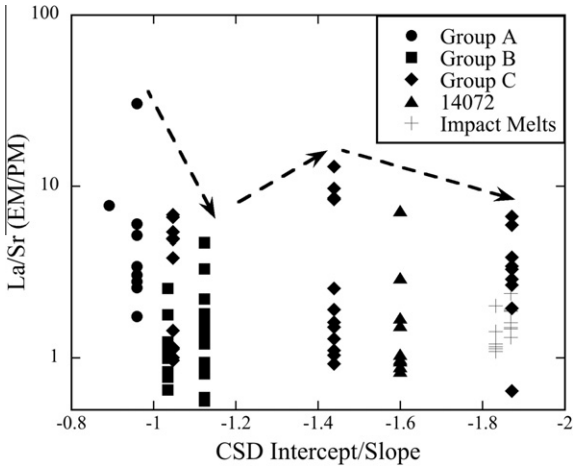

Fig. 14. Correlation between CSD intercept/slope and ratio of plagioclase-equilibrium-melt (EM) La/Sr and parental-melt (PM) La/Sr. Parental-melt compositions are from Neal and Kramer (2006).

A basalts (Fig. 3), as indicated by their steeper CSDs, could mean that assimilation of lunar regolith during lava flow across the lunar surface was minor and only seen in the final crystallization of plagioclase. Such minor assimilation was effectively diluted below detection when whole-rock data are considered. Furthermore, faster cooling left less time for assimilant composition to diffuse into the Group A lava. Thus Group A basalts have a generally larger variation of trace-element ratios as depicted by plagioclase equilibrium liquid compositions relative to those in the parental melt, compared to other pristine high-Al basalt groups (Fig. 14). The cooling rates of Group B and C basalts, and basalt 14072 were slower than that of Group A basalts. As such, trace elements from the assimilant(s) had more time to equilibrate in the magma. The variations of trace-element ratios in these basalts are smaller, but they are still larger than that of impact melts (Fig. 14), which evolved though closed-system fractional crystallization. Slower cooling of Group B and C basalts could facilitate more assimilation relative to Group A basalts, as evidenced by whole-rock trace-element modeling (Neal and Kramer, 2006).

The Apollo 14 high-Al basalts exhibit a general relationship between the whole-rock trace-element data and the associated CSDs (Fig. 15). There are two possibilities to explain this variation. One is that this occurred randomly, with each group of basalts having its own ranges of trace element ratios and different crystallization regimes. Another

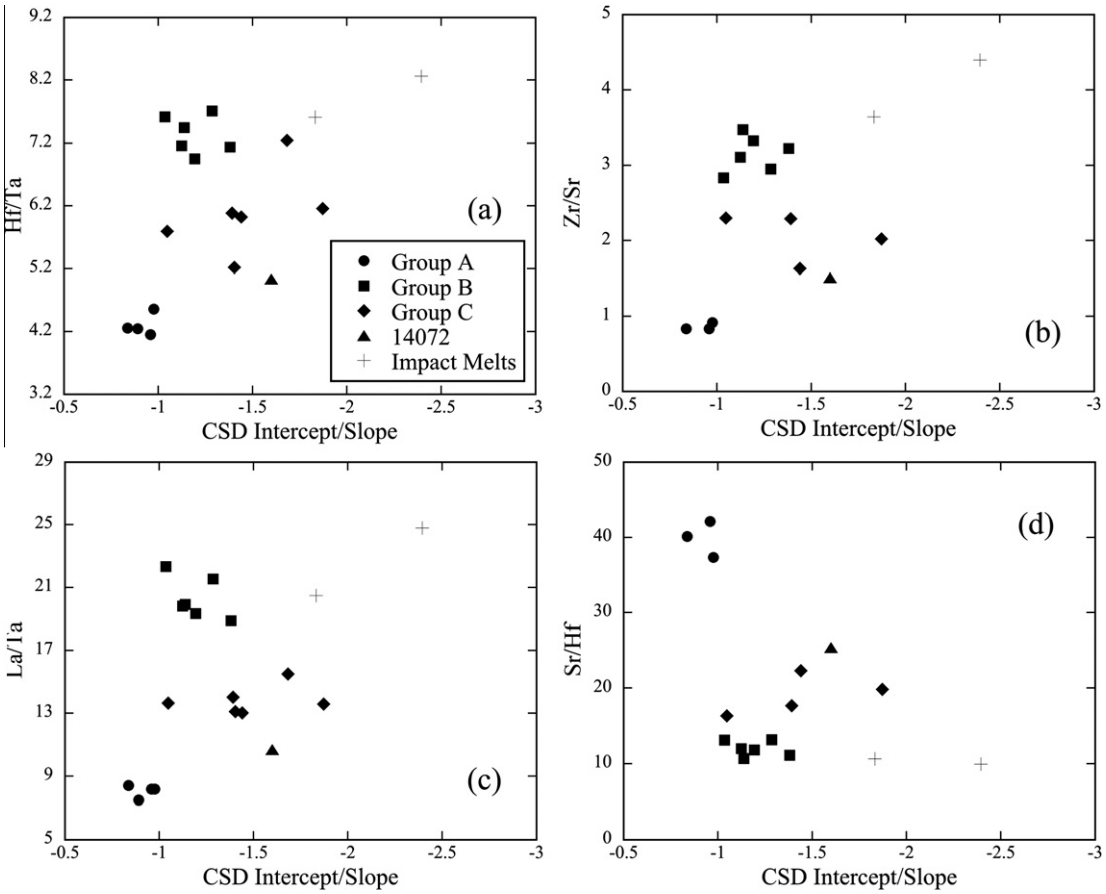

Fig. 15. Whole-rock incompatible-trace-element ratio versus CSD intercept/slope. Variations are caused by faster cooling rates (negating efficient diffusion of assimilant throughout the remaining melt), and more extensive assimilation. See text for discussion. Data sources for whole-rock trace element compositions: Neal and Kramer, 2006 (all the samples in this study except: Group A basalt 14321, 1763; Group C basalts 14321, 9080, 14321, 9057, and 14321, 18; and Impact Melts 14073, 16 and 14276, 54); Dickinson et al., 1985 (14321, 1763, 14321, 9080 and 14321, 9057); Laul et al., 1972 (14073, 3); Vaniman and Papike, 1980 (14276).

explanation is that this is due to inherent crystallization dynamics linking cooling rate and the geochemical composition (e.g., Lange et al., 1994; Dunbar et al., 1995). Examination of other pristine lunar basalts using crystal stratigraphy is necessary to further explore the correlations depicted in Fig. 15.

4.5. Implications for the source regions of high-Al basaltic melts

The origin of the "high alumina" nature of Apollo 14 high-Al basalts has been debated for years. Recent laboratory experiments indicate that anorthosite dissolution may play an important role in the petrogenesis of the high-Al basalts and the "high alumina" characteristics were from lunar anorthosite (Morgan et al., 2006). However, Neal and Kramer (2006) used incompatible-trace-element ratios of the high-Al mare basalts to show that incorporation of feldspathic lunar crustal material is not responsible for the "high alumina" nature of the pristine Apollo 14 basalts. Although feldspathic highland crust (anorthosite) may have been present in the regolith across which the pristine high-Al basalts flowed, it would be a minor component of the actual assimilant because anorthosite has a higher melting temperature relative to KREEP and granite and such a "selective" assimilation may occur during lava flow on the lunar surface. This conclusion inferred from the melting process is supported by the fact that such a component would have a higher Sr concentration and smaller La/Sr ratio (Sr = 210–560 ppm, La/Sr = 0.015–0.96, Warren et al., 1983b, 1987; Lindstrom et al., 1984; Goodrich et al., 1986) compared to the estimated assimilant compositions (Table 3) that would produce the observed plagioclase-equilibrium-melt compositions. We therefore support the conclusion of Neal and Kramer (2006) that the "high alumina" signature of the pristine Apollo 14 basalts is not generated by assimilation of anorthosite-rich lunar crustal material. The "high alumina" nature must be inherited from the mantle sources (e.g., partial melting of a hybrid mantle, Hagerty et al., 2005), which controlled parental melt compositions.

The impact melts studied here are also enriched in alumina. The impact melts are typically the product of crystallization of impact-melted lunar regolith and/or part of the feldspathic lunar crust (e.g., Schonfeld and Meyer, 1972). In contrast to the pristine basalts, the origin of the "high alumina" signature of the impact melts is inherited from the lunar anorthosite. This is consistent with the slightly higher modal abundances of plagioclase in the impact melts (Table 1; Fig. 5b and c), which produce plagioclase as one of the first liquidus phases from the melts (Table 6, Gancarz et al., 1972). This is also consistent with the compositional differences between the pristine and impact high-Al melts noted by Neal and Kramer (2006).

5. SUMMARY

Textural analyses of the Apollo 14 high-Al basaltic melts support the idea that the basalt clasts from breccia 14321 and the basaltic hand specimen sample 14072 are distinct from the impact melts and also comprise at least three unique groups. The pristine basalts (14072, Groups A, B, C) and the impact melts occupy different ranges of characteristic lengths and plagioclase abundances (Fig. 5b), suggesting that the melts of each group had unique cooling histories. The CSD of basalt 14072 falls in the range of Group C.

Investigation of the petrogenesis of Apollo 14 high-Al basaltic melts using a crystal stratigraphy approach has revealed insights into how the basalts crystallized that were not evident from whole-rock trace-element data. Petrogenetic modeling of trace-element variations in plagioclase crystals from Group A basalts reveals that crystallization involved open-system AFC processes at the end of crystallization, contrasting with the whole-rock studies that suggested a closed-system magma evolution. Trace element modeling of individual crystals from Group B and C basalts also offers more insight into the respective petrogenesis than the whole-rock data alone. In both of these groups the equilibrium-melt compositions do not fall on a single AFC trajectory, thus suggesting that r-values and/or assimilant compositions fluctuated during magma evolution (Figs. 9 and 10). Petrogenetic modeling of basalt 14072 using plagioclase compositions reveals that it also experienced an assimilation and fractional crystallization process (Fig. 11). In contrast to the pristine basalts, petrogenesis of the impact melts can be explained by closed-system fractional crystallization (Fig. 12). The petrogenetic modeling suggests that the pristine basaltic melts continued to evolve as they flowed across KREEP/granite-rich regolith on the lunar surface in the Imbrium region, but impact melts crystallized in a more static environment, such as thicker impact-generated melt sheets that did not flow very far (i.e., were trapped within the impact crater). The geologic settings are consistent with the cooling histories inferred from their CSD analyses. The plagioclase data of the Apollo 14 basaltic melts from this study suggest that AFC processes only occurred when the magma flowed across the lunar surface. The petrogenetic modeling of the pristine Apollo 14 high-Al basalts supports that "high alumina" nature has been imparted from their source regions.

This study demonstrates that whole-rock petrogenetic modeling of Apollo 14 high-Al basalts gives a more general idea of the basalt evolution, in that compositions are averaged during the homogenization of the whole-rock sample. This produces average values for assimilation-to-crystallization ratios and assimilant compositions that occurred during magma evolution, or if assimilation was minor, the whole-rock "average" composition may miss it altogether. Therefore the use of compositional trends across individual crystals reveals the complexities of magma evolution and gives more details regarding melt petrogenesis. This study demonstrates that crystal stratigraphy yields important insights into melt evolution that cannot be seen using whole-rock data and is a novel approach in studying petrogenesis of lunar basalts.

ACKNOWLEDGEMENTS

This research was supported by NASA Grant NNG06-GF11G to Clive R. Neal. We would like to acknowledge John Shafer and

Tony Simonetti for help with the LA-ICP-MS, and Brad Jolliff and Paul Carpenter of Washington University for help with the electron microprobe. We thank Christian Koeberl for editorial handling as well as insightful comments, Ryan Ziegler and an anonymous reviewer for constructive and detailed reviews.

APPENDIX A. SUPPLEMENTARY DATA

Supplementary data associated with this article can be found, in the online version, at doi:10.1016/j.gca.2011.08.015.

REFERENCES

Aigner-Torres M., Blundy J., Ulmer P. and Pettke T. (2007) Laser ablation ICP-MS study of trace element partition between plagioclase and basaltic melts: An experimental approach. *Contrib. Mineral. Petrol.* **153**, 647–667.

Anand M., Taylor L. A., Floss C., Neal C. R., Terada K. and Tanikawa S. (2006) Petrology and geochemistry of LaPaz Icefield 02205: a new unique low-Ti mare-basalt meteorite. *Geochim. Cosmochim. Acta* **70**, 246–264.

Armstrong J. T. (1995) CITZAF: a package of correction programs for the quantitative electron microbeam X-ray analysis of thick polished materials, thin films, and particles. *Microbeam Anal.* **4**, 177–200.

Bédard J. H. (2001) Parental magmas of the Nain Plutonic Suite anorthosites and mafic cumulates: a trace element modeling approach. *Contrib. Mineral. Petrol.* **141**, 747–771.

Bédard J. H. (2006) Trace element partitioning in plagioclase feldspar. *Geochim. Cosmochim. Acta* **70**, 3717–3742.

Bindeman I. N. and Davis A. M. (2000) Trace element partitioning between plagioclase and melt: investigation of dopant influence on partition behavior. *Geochim. Cosmochim. Acta* **64**, 2863–2878.

Bindeman I. N., Davis A. M. and Drake M. J. (1998) Ion microprobe study of plagioclase-basalt partition experiments at natural concentration levels of trace elements. *Geochim. Cosmochim. Acta* **62**, 1175–1193.

Blundy J. (1997) Experimental study of a Kiglapait marginal rock and implications for trace element partitioning in layered intrusions. *Chem. Geol.* **141**, 73–92.

Blundy J. D. and Wood B. J. (1991) Crystal-chemical controls on the partitioning of Sr and Ba between plagioclase feldspar, silicate melts, and hydrothermal solutions. *Geochim. Cosmochim. Acta* **55**, 193–209.

Brunfelt A. O., Heier K. S., Nilssen B. and Sundvoll B. (1972) Distribution of elements between different phases of Apollo 14 rocks and soils. *Proc. Lunar Sci. Conf.* **3**, 1133–1147.

Crisp J. and Baloga S. (1994) Influence of crystallization and entrainment of cooler material on the emplacement of basaltic aa lava flows. *J. Geophys. Res.* **99**, 11819–11831.

Dasch E. J., Shih C.-Y., Bansal B. M., Wiesmann H. and Nyquist L. E. (1987) Isotopic analysis of basaltic fragments from lunar breccia 14321: chronology and petrogenesis of pre-Imbrium mare volcanism. *Geochim. Cosmochim. Acta* **51**, 3241–3254.

DePaolo D. (1981) Trace element and isotopic effects of combined wallrock assimilation and fractional crystallization. *Earth Planet. Sci. Lett.* **53**, 189–202.

Dickinson T., Taylor G. T., Keil K., Schmitt R. A., Hughes S. S. and Smith M. R. (1985) Apollo 14 aluminous mare basalts and their possible relationship to KREEP. *Proc. Lunar Planet. Sci. Conf.* **15**, C365–C374.

Dunbar N. W., Jacobs G. K. and Naney M. T. (1995) Crystallization processes in an artificial magma: variations in crystal shape, growth rate and composition with melt cooling history. *Contrib. Mineral. Petrol.* **120**, 412–425.

Dungan M. A. and Brown R. W. (1977) The petrology of the Apollo 12 ilmenite basalt suite. *Proc. Lunar Sci. Conf.* **8**, 1339–1381.

Gancarz A. J., Albee A. L. and Chodos A. A. (1971) Petrologic and mineralogic investigation of some crystalline rocks returned by the Apollo 14 mission. *Earth Planet. Sci. Lett.* **12**, 1–18.

Gancarz A. J., Albee A. L. and Chodos A. A. (1972) Comparative petrology of Apollo 16 sample 68415 and Apollo 14 samples 14276 and 14310. *Earth Planet. Sci. Lett.* **16**, 307–330.

Ghiorso M. S. and Sack R. O. (1995) Chemical mass transfer in magmatic processes. IV. A revised and internally consistent thermodynamic model for the interpolation and extrapolation of liquid–solid equilibria in magmatic systems at elevated temperatures and pressures. *Contrib. Mineral. Petrol.* **119**, 197–212.

Goodman R. J. (1972) The distribution of Ga and Rb in coexisting groundmass and phenocryst phases of some basic volcanic rocks. *Geochim. Cosmochim. Acta* **36**, 303–317.

Goodrich C. A., Taylor G. J., Keil K., Kallemeyn G. W. and Warren P. H. (1986) Alkali norite, troctolites, and VHK mare basalts from breccia 14304. *Proc. Lunar Planet. Sci. Conf.* **16**, D305–D318.

Griffiths R. W. (2000) The dynamics of lava flows. *Annu. Rev. Fluid Mech.* **32**, 477–518.

Hagerty J. J., Shearer C. K. and Papike J. J. (2005) Petrogenesis of the Apollo 14 high-alumina basalts: Implications from ion microprobe analyses. *Geochim. Cosmochim. Acta* **69**, 5831–5845.

Haggerty S. E. (1978) The redox state of planetary basalts. *Geophys. Res. Lett.* **5**, 443–446.

Helmke P. A., Haskin L. A., Korotev R. L. and Ziege K. E. (1972) Rare earths and other trace elements in Apollo 14 samples. *Proc. Lunar Sci. Conf.* **3**, 1275–1292.

Hersum T. G. and Marsh B. D. (2007) Igneous textures: on the kinetics behind the words. *Elements* **3**, 247–252.

Higgins M. D. (1996) Magma dynamics beneath Kameni volcano, Thera, Greece, as revealed by crystal size and shape measurements. *J. Volcanol. Geoth. Res.* **70**, 37–48.

Higgins M. D. (2000) Measurement of crystal size distributions. *Am. Mineral.* **85**, 1105–1116.

Higgins M. D. (2002) Closure in crystal size distributions (CSD), verification of CSD calculations, and the significance of CSD fans. *Am. Mineral.* **87**, 171–175.

Higgins M. D. (2011a) Textural coarsening in igneous rocks. *Int. Geol. Rev.* **53**, 354–376.

Higgins M.D. (2011b) Quantitative petrological evidence for the origin of K-feldspar megacrysts in dacites from Taapaca volcano, Chile. *Contrib. Mineral. Petrol.* Published on-line March 10, 2011. DOI 10.1007/s00410-011-0620-9.

Higgins M. D. and Roberge J. (2003) Crystal size distribution of plagioclase and amphibole from Soufrière Hills Volcano, Montserrat: Evidence for dynamic crystallization-textural coarsening cycles. *J. Petrol.* **44**, 1401–1411.

Hubbard N. J., Gast P. W., Rhodes J. M., Bansal B. M., Wiesmann H. and Church S. E. (1972) Nonmare basalts: Part II. *Proc. Lunar Sci. Conf.* **3**, 1161–1179.

Hulme G. (1982) A review of lava flow processes related to the formation of lunar sinuous rilles. *Geophys. Surv.* **5**, 245–279.

Jolliff B. L. (1991) Fragments of quartz monzodiorite and felsite in Apollo 14 soil particles. *Proc. Lunar Planet. Sci. Conf.* **21**, 101–118.

Kauahikaua J., Cashman K. V., Mattox T. N., Heliker C. C., Hon K. A., Mangan M. T. and Thornber C. R. (1998) Observations on basaltic lava in tubes from Kilauea Volcano, island of Hawai'i. *J. Geophys. Res.* **103**, 27303–27323.

Keszthelyi L. and Self S. (1998) Some physical requirements for the emplacement of long basaltic lava flows. *J. Geophys. Res.* **103**, 27447–27464.

Lange R. A., Cashman K. V. and Navrotsky A. (1994) Direct measurements of latent heat during crystallization and melting of a ugandite and an olivine basalt. *Contrib. Mineral. Petrol.* **118**, 169–181.

Laul J. C., Wakita H., Showalter D. L., Boynton W. V. and Schmitt R. A. (1972) Bulk, rare earth, and other trace elements in Apollo 14 and 15 and Luna 16 samples. *Proc. Lunar Sci. Conf.* **3**, 1181–1200.

Lesher C. M. and Campbell I. H. (1993) Geochemical and fluid dynamic modeling of compositional variations in Archean komatiite-hosted nickel sulfide ores in Western Australia. *Econ. Geol.* **88**, 804–816.

Lindstrom M. M., Knapp S. A., Shervais J. W. and Taylor L. A. (1984) Magnesian anorthosites and associated troctolites and dunite in Apollo 14 breccias. *Proc. Lunar Planet. Sci. Conf.* **15**, C41–C49.

Longhi J., Walker D. and Hays J. F. (1972) Petrography and crystallization history of basalts 14310 and 14072. *Proc. Lunar Sci. Conf.* **3**, 131–139.

Mark R. K., Cliff R. A., Lee-Hu C. and Wetherill G. W. (1973) Rb–Sr studies of lunar breccias and soils. *Proc. Lunar Sci. Conf.* **4**, 1785–1795.

Mark R. K., Lee-Hu C. and Wetherill G. W. (1974) Equilibration and ages: Rb–Sr studies of breccias 14321 and 15265. *Proc. Lunar Sci. Conf.* **5**, 1477–1485.

Mark R. K., Lee-Hu C. and Wetherill G. W. (1975) More on Rb–Sr in lunar breccia 14321. *Proc. Lunar Sci. Conf.* **6**, 1501–1507.

Marsh B. D. (1988) Crystal size distribution (CSD) in rocks and the kinetics and dynamics of crystallization I. Theory. *Contrib. Mineral. Petrol.* **99**, 277–291.

Marsh B. D. (1998) On the interpretation of crystal size distributions in magmatic systems. *J. Petrol.* **39**, 553–599.

Masuda A., Nakamura N., Kurasawa H. and Tanaka T. (1972) Precise determination of rare-earth elements in the Apollo 14 and 15 samples. *Proc. Lunar Sci. Conf.* **3**, 1307–1313.

McKay G. A. and Weill D. F. (1977) KREEP petrogenesis revisited. *Proc. Lunar Planet. Sci. Conf.* **8**, 2339–2355.

Meyer C. (1977) Petrology, mineralogy, and chemistry of KREEP basalt. *Phys. Chem. Earth* **10**, 239–260.

Morgan D. J. and Jerram D. A. (2006) On estimating crystal shape for crystal size distribution analysis. *J. Volcanol. Geoth. Res.* **154**, 1–7.

Morgan Z., Liang Y. and Hess P. (2006) An experimental study of anorthosite dissolution in lunar picritic magmas: Implications for crustal assimilation processes. *Geochim. Cosmochim. Acta* **70**, 3477–3491.

Murase T. and McBirney A. R. (1970) Viscosity of lunar lavas. *Science* **167**, 1491–1493.

Neal C. R. and Kramer G. Y. (2006) The petrogenesis of the Apollo 14 high-Al mare basalts. *Am. Mineral.* **91**, 1521–1535.

Neal C. R. and Taylor L. A. (1990) Modeling of lunar basalt petrogenesis: Sr isotope evidence from Apollo 14 high-alumina basalts. *Proc. Lunar Planet. Sci. Conf.* **20**, 101–108.

Neal C. R. and Taylor L. A. (1991) Evidence for metasomatism of the Lunar Highlands and the origin of whitlockite. *Geochim. Cosmochim. Acta* **55**, 2965–2980.

Neal C. R. and Taylor L. A. (1992) Petrogenesis of mare basalts: a record of lunar volcanism. *Geochim. Cosmochim. Acta* **56**, 2177–2211.

Neal C. R., Taylor L. A. and Lindstrom M. M. (1988) Apollo 14 mare basalt petrogenesis: assimilation of KREEP-like components by a fractionating magma. *Proc. Lunar Planet. Sci. Conf.* **18**, 139–153.

Neal C. R., Taylor L. A., Schmitt R. A., Hughes S. S. and Lindstrom M. M. (1989a) High alumina (HA) and very high potassium (VHK) basalt clasts from Apollo 14 breccias, Part 2 – Whole rock chemistry: Further evidence for combined assimilation and fractional crystallization within the lunar crust. *Proc. Lunar Sci. Conf.* **19**, 147–161.

Neal C. R., Taylor L. A. and Patchen A. D. (1989b) High alumina (HA) and very high potassium (VHK) basalt clasts from Apollo 14 Breccias, Part 1—Mineralogy and petrology: evidence of crystallization from evolving magmas. *Proc. Lunar Planet. Sci. Conf.* **19**, 137–145.

O'Connell-Cooper C. D. and Spray J. G. (2011) Geochemistry of the impact-generated melt sheet at Manicouagan: evidence for fractional crystallization. *J. Geophys. Res.* **116**, B06204, doi:10.1029/2010JB008084.

Papanastassiou D. A. and Wasserburg G. J. (1971) Rb–Sr ages of the igneous rocks from the Apollo 14 mission and the age of the Fra Mauro Formation. *Earth Planet. Sci. Lett.* **12**, 36–48.

Papike J. J. and Bence A. E. (1978) Lunar Mare versus terrestrial mid-ocean ridge basalts: planetary constraints on basaltic volcanism. *Geophys. Res. Lett.* **5**, 803–806.

Papike J. J., Hodges F. N., Bence A. E., Cameron M. and Rhodes J. M. (1976) Mare basalts: crystal chemistry, mineralogy and petrology. *Rev. Geophys. Space Phys.* **14**, 475–540.

Philpotts J. A., Schnetzler C. C., Nava D. F., Bottino M. L., Fullagar P. D., Thomas H. H., Schuhmann S. and Kouns C. W. (1972) Apollo 14: Some geochemical aspects. *Proc. Lunar Sci. Conf.* **3**, 1293–1305.

Prowatke S. and Klemme S. (2006) Trace element partitioning between apatite and silicate melts. *Geochim. Cosmochim. Acta* **70**, 4513–4527.

Ridley W. I. (1975) On high-alumina mare basalts. *Proc. Lunar Sci. Conf.* **6**, 131–145.

Ridley W. I., Brett R., Williams R. J., Takeda H. and Brown R. W. (1972) Petrology of Fra Mauro basalt 14310. *Proc. Lunar Sci. Conf.* **3**, 159–170.

Rose, Jr., H. J., Cuttitta F., Annell C. S., Carron M. K., Christian R. P., Dwornik E. J., Greenland L. P. and Ligon, Jr., D. T. (1972) Compositional data for twenty-one Fra Mauro lunar materials. *Proc. Lunar Sci. Conf.* **3**, 1215–1229.

Ryder G. (1976) Lunar sample 15405: Remnant of a KREEP basalt-granite differentiated pluton. *Earth Planet. Sci. Lett.* **29**, 255–268.

Sato M., Hickling N. L. and McLane J. E. (1973) Oxygen fugacity values of Apollo 12, 14, and 15 lunar samples and reduced state of lunar magmas. *Proc. Lunar Sci. Conf.* **4**, 1061–1079.

Schonfeld E. and Meyer, Jr., C. (1972) The abundances of components of the lunar soils by a least-squares mixing model and the formation age of KREEP. *Proc. Lunar Sci. Conf.* **3**, 1397–1420.

Shearer C. K., Hess P. C., Wieczorek M. A., Pritchard M. E., Parmentier E. M., Borg L. E., Longhi J., Elkins-Tanton L. T., Neal C. R., Antonenko I., Canup R. M., Halliday A. N., Grove T. L., Hager B. H., Lee D.-C. and Wiechert U. (2006) Thermal and magmatic evolution of the Moon. *Rev. Mineral. Geochem.* **60**, 365–518.

Shervais J. W., Taylor L. A. and Lindstrom M. M. (1985) Apollo 14 mare basalts: Petrology and geochemistry of clasts from consortium breccia 14321. *Proc. Lunar Planet. Sci. Conf.* **15**, C375–C395.

Snyder G.A., Borg L.E., Nyquist L.E. and Taylor L.A. (2000) Chronology and isotopic constraints on lunar evolution. In

Origin of the Earth and Moon (eds. R.M. Canup and K. Righter). Univ. Arizona Press. pp. 361–395.

Snyder G. Y., Taylor L. A. and Neal C. R. (1992) A chemical model for generating the sources of mare basalts: combined equilibrium and fractional crystallization of the lunar magmasphere. *Geochim. Cosmochim. Acta* **56**, 3809–3823.

Taylor S. R., Kaye M., Muir P., Nance W., Rudowski R. and Ware N. (1972) Composition of the lunar uplands: chemistry of Apollo 14 samples from Fra Mauro. *Proc. Lunar Sci. Conf.* **3**, 1231–1249.

Tepley, III, F. J., Lundstrom C. C., McDonough W. F. and Thompson A. (2010) Trace element partitioning between high-An plagioclase and basaltic to basaltic andesite melt at 1 atmosphere pressure. *Lithos* **118**, 82–94.

Vaniman D. T. and Papike J. J. (1980) Lunar highland melt rocks: chemistry, petrology and silicate mineralogy. In *Proceedings of the Conference on the Lunar Highlands Crust* (eds. J. J. Papike and R. B. Merrill). Pergamon Press, New York and Oxford, pp. 271–337.

Warren P. H. (1993) A concise compilation of petrologic information on possibly pristine nonmare Moon rocks. *Am. Mineral.* **78**, 360–376.

Warren P. H. and Kallemeyn G. W. (1984) Pristine rocks (8th Foray): "Plagiophile" element ratios, crustal genesis, and the bulk compositions of the moon. *Proc. Lunar Planet. Sci. Conf.* **5**, C16–C24.

Warren P. H. and Wasson J. T. (1979) The origin of KREEP. *Rev. Geophys. Space Phys.* **17**, 73–88.

Warren P. H., Jerde E. A. and Kallemeyn G. W. (1987) Pristine moon rocks: a "large" felsite and a metal-rich ferroan anorthosite. *Proc. Lunar Planet. Sci. Conf.* **17**, E303–E313.

Warren P. H., Taylor G. J., Keil K., Shirley D. N. and Wasson J. T. (1983a) Petrology and chemistry of two "large" granite clasts from the Moon. *Earth Planet. Sci. Lett.* **64**, 175–185.

Warren P. H., Taylor G. J., Keil K., Kallemeyn G. W., Shirley D. N. and Wasson J. T. (1983b) Seventh Foray: Whitlockite-rich lithologies, a diopside-bearing troctolitic anorthosite, ferroan anorthosite, and KREEP. *Proc. Lunar Planet. Sci. Conf.* **14**, B151–B164.

Weill D. F. and McKay G. A. (1975) The partitioning of Mg, Fe, Sr, Ce, Sm, Eu, and Yb in lunar igneous systems and possible origin of KREEP by equilibrium partial melting. *Proc. Lunar Planet. Sci. Conf.* **6**, 1143–1158.

Willis J. P., Erlank A. J., Gurney J. J., Theil R. H. and Ahrens L. H. (1972) Major, minor, and trace element data for some Apollo 11, 12, 14, and 15 samples. *Proc. Lunar Sci. Conf.* **3**, 1269–1273.

Zieg M. J. and Marsh B. D. (2002) Crystal size distributions and scaling laws in the quantification of igneous textures. *J. Petrol.* **43**, 85–101.

Associate editor: Christian Koeberl